

Siles-Ajamil, R., Díez-Minguito, M., & Losada, M. Á. (2019). Tide propagation and salinity distribution response to changes in water depth and channel network in the Guadalquivir River Estuary: An exploratory model approach. *Ocean & Coastal Management*, 174, 92-107. Under license: CC BY-NC-ND
Link to publisher version with DOI: <https://doi.org/10.1016/j.ocecoaman.2019.03.015>

Tide propagation and salinity distribution response to changes in water depth and channel network in the Guadalquivir River Estuary: An exploratory model approach

R. Siles-Ajamil^{a,*} M. Díez-Minguito^a M.Á. Losada^a

^a *Andalusian Institute for Earth System Research. University of Granada. CEAMA, Avda. del Mediterráneo, s/n, 18006 Granada, Spain*

Abstract

This study analyzes the management alternatives that are currently considered by public administrations in the Guadalquivir River Estuary, which is a well-mixed and rather channelized estuary in the southwest of Spain. A linearized multichannel exploratory model that operates at tidal and averaged scales is used. The model extends the previous developments for calculating the tidal variations of salinity and provides elevations, currents and salinity. The effects of the change in mean depth of the main navigation channel, the reconnection of a secondary tidal channel (Brazo del Oeste) and the recovery of a marsh in the lower part of the estuary are the three alternatives analyzed. The model outputs indicate that the channel deepening would produce an increase in the amplitudes of the elevations, tidal salinities, and tidal prisms, as well as the extent of the saline intrusion. Similar effects could be alternatively obtained with the reconnection of the secondary channel with suitable

*corresponding author: reyess@ciccp.es

design parameters. The increase in tidal elevations due to channel deepening should therefore be considered in any dredging project, because lower sediment volumes need to be dredged to attain the projected water column height at high water. The recovery of marshes notably influences the tidal wave propagation when the connecting width with the navigation channel exceeds one hundred meters. Its most remarkable effect is to increase the tidal amplitudes and to reduce the tidal currents upstream the connection point in proportion to the degree of connectivity with the main channel. A combination of alternatives could potentially serve to mitigate the specific effects of individual alternatives. The effects of channel deepening on the amplitudes of the tidal elevation and the currents could be partially compensated for through the recovery of tidal marshes.

Keywords: tides, salinity, multichannel model, channel deepening, marsh recovery

1 1. Introduction

2 Estuaries are coastal systems that are characterized by the exchange of
3 energy, salt, sediments and other substances between the sea and the river
4 basin (Geyer and MacCready, 2014). These systems shelter some of the
5 most productive ecosystems on Earth that support important environmental,
6 social and economic activities.

7 In addition to natural exchange processes, human activities can alter
8 the hydrodynamics, morphology and water quality of estuaries. Estuaries
9 have been dredged with ever greater intensity since the 19th century. Their
10 original water courses have been modified with channeling and short-cutting

11 meanders to favor navigation. Estuarine intertidal areas and marshes are
12 occupied to give them new uses. Dams are constructed to regulate irrigation
13 and reduce the risk of flooding. Competition for the use of resources results
14 in environmental and socioeconomic conflicts, which require intervention by
15 administrative bodies that implement coordination and management plans
16 (Clark, 1997; Stepanova, 2015). However, to adopt suitable and coordinated
17 solutions, these administrative bodies require appropriate tools to diagnose
18 and assess the consequences of human interventions in estuarine systems.
19 For this purpose, idealized models emerge as valuable tools, because they
20 are versatile enough to explore and quantify the effects of different human
21 interventions (e.g. Cai et al., 2012; Schuttelaars et al., 2013). Idealized, ex-
22 ploratory models are simple and fast enough to provide a primary evaluation
23 of trends and guide more detailed studies with more complex computational
24 models (e.g. van Maren et al., 2015; Zarzuelo et al., 2018).

25 A prototypical estuarine system in which there are often conflicts is the
26 Guadalquivir River Estuary (GRE) (Fig. 1). The intensification of human
27 pressure in recent decades, combined with a failure to apply the current scien-
28 tific knowledge in decision-making processes, has resulted in ever-increasing
29 socioeconomic and environmental problems (Ruiz et al., 2015). Agriculture
30 and other soil demands have eliminated most of the marshes, which existed
31 until the twentieth century (González Arteaga et al., 1993). Meanders and
32 secondary channels were cut, and the main channel was deepened with a
33 goal of improving navigation to the inland Port of Seville (del Moral Ituarte,
34 1991). These modifications altered tidal propagation and the distribution
35 of sediment and salt. Additionally, the modifications shifted the estuary to



Figure 1: Study area. The map includes the monitoring stations used in this work. Tidal gauges are located in the main channel, $\beta_{m,i}$, and in the access channel to the Port of Seville, $\beta_{s,i}$. Environmental quality stations or CTDs are denoted by $\gamma_{m,i}$. Current meters are denoted by $\alpha_{m,i}$. See (Navarro et al., 2011) for more details. The stars indicate the position of the nodes for the idealized model ($\star, n_{j,k}$). The origin of the coordinates, which is located at the mouth of the estuary ($x = 0$ km, positive upstream), is established at node $n_{m,0}$, which coincides with the tidal gauge $\beta_{m,0}$ located at the Port of Bonanza.

36 a hyper-turbid state and transformed it into a one single channel, which
 37 was isolated from the surrounding natural areas (Fig. 1), particularly from
 38 Doñana National Park.

39 To partly restore the GRE to previous conditions, a number of scenarios
 40 are currently being considered or promoted by different public administrative
 41 bodies. Outstanding projected management scenarios are as follows:

- 42 • Deepening/shallowing of the navigation channel (Scenario 1),
- 43 • Reconnection of the longest secondary tidal channel (known as Brazo
 44 del Oeste) (Scenario 2), and
- 45 • Recovery of marshes in the lower part of the estuary (Scenario 3).

46 Therefore, within this context, the main aim of this study is to evalu-
 47 ate the impact of these three projected management scenarios on the tidal

48 propagation and salinity distribution and discuss their consequences in the
49 estuarine system.

50 This aim is carried out with a linearized and multichannel idealized model,
51 which couples the shallow-water equations for elevations and currents with
52 the longitudinal one-dimensional salt transport equation. The analysis is
53 specifically focused on the M2 tidal elevations and currents, the longitudi-
54 nal mean distribution of salinity, and the M2 tidal amplitude of salinity.
55 Classical solutions for the linearized shallow-water equations are employed
56 for tidal propagation (Officer, 1976) and set up for stretches in the channel
57 network of the GRE. Exact analytical solutions for the amplitudes of tidal
58 salinity are obtained using the Prandle (1981) approach. These solutions
59 are derived from the longitudinal advection-dispersion equation for salinity.
60 The current hydrodynamic conditions and morphology of the GRE are as-
61 sumed as the reference configuration from which to analyze the impacts of
62 the three scenarios. With these conditions, the model is properly calibrated
63 with hydrodynamic and salinity data.

64 This study is inspired by previous studies in other estuaries and in the
65 GRE itself. Simple tidal models with linearized friction were considered by
66 various authors, such as van Rijn (2011); Cai et al. (2012); Alebregtse et al.
67 (2013); Li et al. (2016). Other works by Wong (1991) in the Delaware estuary,
68 Souza and Hill (2006); Hill and Souza (2006) in the Queen Charlotte Sound,
69 Lugt (2012) in the Ems estuary, and Garel and Cai (2018) in the Guadiana
70 estuary provided analytical solutions that allow for an evaluation of the tidal
71 dynamics in complex channel networks. Prandle and Rahman (1980) and
72 Prandle (1981) developed analytical solutions that enabled the evaluation

73 of the influence of barriers in tidal propagation and in the distribution of
74 mean longitudinal salinity, respectively. In the GRE, previous studies were
75 also carried out. Álvarez et al. (2001) considered a unidimensional linear
76 model to study the effect of partial tidal reflection in the channel of the Port
77 of Seville. Contreras (2009) extended the analysis up to the Alcalá del Río
78 Dam, although this author adopted a heuristic approach to include the effect
79 of friction. Recently, Cai et al. (2016) focused on the resonance conditions
80 in the GRE.

81 This paper is organized as follows. Section 2, Materials and Methods,
82 includes a description of the idealized model, its setup and calibration in the
83 Guadalquivir estuary, and a description of the three management scenarios
84 considered. In Section 3, the evaluation and analysis of the impacts on
85 tidal propagation and salinity distribution from each scenario are presented.
86 Discussion of the reach of the results and their possible consequences for
87 the management of the estuary is carried out in Section 4. Finally, the
88 conclusions are summarized in Section 5.

89 **2. Materials and Methods**

90 *2.1. Model*

91 The linearized one-dimensional shallow-water equations are described by
92 the following conservation of mass and momentum equations (Officer, 1976)

$$\frac{\partial \eta}{\partial t} + \frac{1}{b} \frac{\partial (hbu)}{\partial x} = 0, \quad (1a)$$

$$\frac{\partial u}{\partial t} + g \frac{\partial \eta}{\partial x} + \frac{r}{h} u = 0. \quad (1b)$$

94 Here, x represents the along-channel coordinate, and t is the time. The
 95 variable $\eta(x, t)$ is the tidal elevation with respect to the mean level h , and
 96 $u(x, t)$ is the averaged tidal current in the cross-section. The channel width
 97 is b , and r is a Lorentz' linearized friction coefficient. According to the
 98 Eqs. 1a and 1b, tide propagation is barotropic, linear ($\eta/h \ll 1$), and without
 99 rotation (i.e., Rossby's deformation radius is small when compared with b)
 100 (e.g. Ianniello, 1977).

101 The salinity field, which is coupled to hydrodynamic Eqs. 1, is described
 102 by the following unidimensional advection-diffusion equation (Prandle, 1981):

$$\frac{\partial s}{\partial t} + u \frac{\partial s}{\partial x} = D \frac{\partial^2 s}{\partial x^2}, \quad (2)$$

103 where $s(x, t)$ is salinity and D is a constant effective dispersion coefficient
 104 that accounts for longitudinal mixing.

105 For a harmonic forcing at $x = 0$ km with frequency $\sigma = 2\pi/T$ (and period
 106 T), the structure of Eqs. 1 and 2 suggest solutions that take the form of the
 107 following:

$$\eta(x, t) = \Re\{\bar{\eta}(x) + \hat{\eta}(x, t)\} = \Re\{\bar{\eta}(x) + Z(x) \exp(-i\sigma t)\}, \quad (3a)$$

$$u(x, t) = \Re\{\bar{u}(x) + \hat{u}(x, t)\} = \Re\{\bar{u}(x) + U(x) \exp(-i\sigma t)\}, \quad (3b)$$

$$s(x, t) = \Re\{\bar{s}(x) + \hat{s}(x, t)\} = \Re\{\bar{s}(x) + S(x) \exp(-i\sigma t)\}, \quad (3c)$$

110 where the bar ($\bar{\xi}$) indicates the time average of a variable ξ , ($\hat{\xi}$) represents
 111 tidal deviations with respect to ($\bar{\xi}$), and $\Re\{\xi\}$ gives the real part of ξ .
 112 Here, Z , U and S are the complex tidal amplitudes of elevation, current
 113 and salinity, respectively. At the averaged scale, dynamics are considered
 114 stationary, i.e., independent of t . For example, considering a uniform stretch

115 with length x_L , width b , and depth h , by using Eqs. 3a-3b in Eqs. 1, an
 116 ordinary second-order differential equation for Z is obtained (Officer, 1976).
 117 From the solution for Z , an analytical expression for U is obtained. These
 118 are given by the following:

$$Z(x) = A \exp(i\kappa x) + B \exp(-i\kappa x) , \quad (4a)$$

119

$$U(x) = \sigma / (\kappa h) (A \exp(i\kappa x) - B \exp(-i\kappa x)) , \quad (4b)$$

120 where κ is a complex wavenumber given by $\kappa = \kappa_0 \sqrt{1 + ir / (\sigma h)}$, and κ_0
 121 is the wavenumber without friction. The solution for $\hat{\eta}$ (as well as for \hat{u})
 122 is interpreted as a linear superposition of two plane waves propagating in
 123 opposite directions. By establishing the boundary conditions, namely, tidal
 124 cooscillation at $x = 0$, i.e., $\hat{\eta}(0, t) = \Re\{Z_0 \exp(-i\sigma t)\}$, and a closed boundary
 125 at $x = x_L$, i.e., $\hat{u}(x_L, t) = 0$, the constants A and B are calculated. The
 126 solutions for the oscillating part of the water level and current field are as
 127 follows:

$$\hat{\eta}(x, t) = \Re\left\{Z_0 \frac{\cos(\kappa(x_L - x))}{\cos(\kappa x_L)} \exp(-i\sigma t)\right\} , \quad (5a)$$

128

$$\hat{u}(x, t) = \Re\left\{-\frac{Z_0 \sigma i \sin(\kappa(x_L - x))}{h\kappa \cos(\kappa x_L)} \exp(-i\sigma t)\right\} . \quad (5b)$$

129 Similarly, using Eqs. 3b-3c in Eq. 2, the tidal component of the salinity
 130 is deduced as follows:

$$\hat{s}(x, t) = \Re\{(x\hat{A} \exp((i\kappa + \lambda)x) - x\hat{B} \exp(-(i\kappa - \lambda)x)) \exp(-i\sigma t)\} \quad (6)$$

131 where $\lambda = Q_d / (bhD)$, with Q_d representing fresh water discharge, and the
 132 coefficients \hat{A} and \hat{B} are constants to be calculated imposing the boundary
 133 conditions at the upper and lower ends of the stretch.

134 The solutions for the averaged components of the elevations, current, and
 135 salinity are derived following Prandle (1981). These are respectively given
 136 by the following:

$$\bar{\eta} = -\frac{f Q_d}{g h b T_{M2} \sqrt{g h}} x + d, \quad (7a)$$

$$\bar{u} = Q_d / (b h), \quad (7b)$$

$$\bar{s} = \delta_2 \exp(\lambda x) + \delta_1 / \lambda, \quad (7c)$$

139 where d , δ_1 , δ_2 are constants obtained applying the boundary conditions, and
 140 f is an effective friction coefficient at the averaged scale.

141 Solutions 5, 6, 7 are applied to the different stretches along which the
 142 Guadalquivir estuary is segmented. Boundary conditions and matching con-
 143 ditions at the junctions are applied to obtain solutions for the whole estuarine
 144 system. Details of the topology layout for each stretch is given in Section 2.2.
 145 The calculation procedure for elevations, currents, and salinities is detailed
 146 and outlined in Appendix A.

147 2.2. Guadalquivir River Estuary

148 2.2.1. Current Configuration of the Estuary

149 The GRE is located in the southwestern region of the Iberian Peninsula
 150 (Fig. 1) and flows into the Gulf of Cádiz (Atlantic Ocean). The main tidal
 151 channel extends 110 km, being weakly convergent from its only mouth in
 152 Sanlúcar de Barrameda to the Alcalá del Río Dam at its head, upstream
 153 from Seville. The Alcalá del Río Dam represents the last monitoring point
 154 for fresh water and the upstream limit of the incoming tide. The GRE is
 155 navigable up to the Port of Seville, at $x = 85$ km from the mouth of the
 156 estuary. The Port is currently accessible from the main channel by a short

157 secondary channel that is ~ 1 km long. The secondary channel is closed
158 at the landward boundary by a lock to prevent tidal oscillations inside the
159 port. The minimum depth in the main channel is 6.5 m, and it is currently
160 maintained through periodic dredging to increase its navigability. In general,
161 there are only a few secondary channels. The secondary channel of the Brazo
162 del Oeste was disconnected upstream from the main channel to contain the
163 saline intrusion (del Moral Ituarte, 1991). Most of the Doñana National Park
164 (Fig. 1) is currently isolated from the tidal oscillations.

165 The fresh water discharges, Q_d , are less than $40 \text{ m}^3/\text{s}$ during 75% of the
166 year (dry periods). Discharges over $400 \text{ m}^3/\text{s}$, which disrupt tidal propaga-
167 tion (Losada et al., 2017), occur due to high river flows or are associated with
168 the need to irrigate land downstream. For low river-flow conditions, the es-
169 tuary is dominated by tides (Díez-Minguito et al., 2012). The Guadalquivir
170 is a mesomareal estuary (tidal range at spring tide ~ 3.5 m) whose main
171 constituent is the M2 tide ($T_{M2} = 12.42$ hours). The tidal propagation dur-
172 ing normal conditions is explained by tidal reflection, friction and the con-
173 vergence of the main channel (Díez-Minguito et al., 2012). Regarding the
174 vertical salinity structure, the estuary is mostly well mixed (Díez-Minguito
175 et al., 2013). The longitudinal distribution of salt is positive, which means
176 that the maximum salinity levels are normally observed near the mouth of
177 the estuary. Losses caused by evaporation are compensated for by the fresh
178 water discharges. The analyses performed in this study assumed normal or
179 low-flow conditions with $Q_d = 40 \text{ m}^3/\text{s}$.

180 *2.2.2. Base Topology*

181 The estuary is segmented into stretches of uniform cross-section. The
182 division is carried out according to the current morphology and the proposed
183 scenarios. Figure 2 shows the layout topology for each scenario in terms of the
184 stretches and nodes considered. The stretches are defined by the following six
185 nodes: $n_{m,0}$, $n_{m,1}$, $n_{m,2}$, $n_{m,3}$, $n_{m,4}$, and $n_{m,5}$. The stretches are denoted from
186 the mouth of the estuary to upstream as $\mathbb{S}_{m,1}$, $\mathbb{S}_{m,2}$, $\mathbb{S}_{m,3}$, $\mathbb{S}_{m,4}$, and $\mathbb{S}_{m,5}$. The
187 subscript m refers to the “main” channel. Figure 1 shows the actual location
188 of each node, and Table 1 shows the physical parameters of each stretch. At
189 the nodes (or connection points), boundary or matching conditions must be
190 fulfilled. The latter are equal elevations and conservation of flow. The M2
191 tide forcing is imposed at the seaward boundary at node $n_{m,0}$. This node is
192 located at the Port of Bonanza (Fig. 1). A closed boundary is considered
193 at the uppermost node $n_{m,5}$. This node coincides with the Alcalá del Río
194 Dam, where total reflection is considered. The secondary tidal channels are
195 denoted with the subscript s . The channel used to access the Port of Seville
196 constitutes the secondary channel defined as $\mathbb{S}_{s,1}$, where the reflection is also
197 considered to be total. The configuration before the construction of the New
198 Lock (Fig. 2a) is used for calibration of the model, because the measurements
199 used to calibrate the model were recorded between 2008 and 2011.

200 Other stretches are defined for the assessment of scenarios 1, 2, and 3
201 (Fig. 2b, 2c, and 2d, respectively). These are $\mathbb{S}_{s,2}$, which corresponds to the
202 New Lock, $\mathbb{S}_{s,3}$, which corresponds to the Brazo del Oeste, and $\mathbb{S}_{s,4}$, $\mathbb{S}_{s,5}$,
203 which corresponds to the recovered marshes in the lower part of the estuary.

Table 1: Values for the parameters at each stretch. Nodes are shown in Fig. 2. Parameters L , b , and h are length, width, and depth, respectively. Friction and diffusion coefficients, r and D , respectively, are adjusted for the M2 constituent.

Stretches	Nodes	L (km)	b (km)	h (m)	$r \times 10^{-3}$	D (m ² /s)
$\mathbb{S}_{m,1}$	$(n_{m,0}, n_{m,1})$	12.0	0.400	6.5	1.9	550.00
$\mathbb{S}_{m,2}$	$(n_{m,1}, n_{m,2})$	6.3	0.350	6.5	1.5	514.29
$\mathbb{S}_{m,3}$	$(n_{m,2}, n_{m,3})$	42.6	0.300	6.5	1.3	514.29
$\mathbb{S}_{m,4}$	$(n_{m,3}, n_{m,4})$	18.1	0.200	6.5	1.0	300.00
$\mathbb{S}_{m,5}$	$(n_{m,4}, n_{m,5})$	24.2	0.100	6.5	1.4	335.71
$\mathbb{S}_{s,1}$	$(n_{m,4}, n_{s,1})$	2.9	0.238	6.5	1.0	300.00
$\mathbb{S}_{s,2}$	$(n_{m,4}, n_{s,2})$	0.8	0.192	6.5	1.0	300.00
$\mathbb{S}_{s,3}$	$(n_{m,2}, n_{m,3})$	56.1	0.350	6.5	1.0	514.29
$\mathbb{S}_{s,4}$	$(n_{m,1}, n_{s,3})$	4.0	0.060	1.0	1.0	550.00
$\mathbb{S}_{s,5}$	$(n_{s,3}, n_{s,4})$	16.0	16	1.0	1.0	550.00

Table 2: The location of tidal gauges, current meters and nodes for the model (see Fig. 1). All values are given in km.

Tidal Gauges		Current Meters		Nodes	
$\beta_{m,0}$	0.00	$\alpha_{m,0}$	9.00	$n_{m,0}$	0.00
$\beta_{m,1}$	16.25	$\alpha_{m,1}$	15.50	$n_{m,1}$	12.00
$\beta_{m,2}$	21.5	$\alpha_{m,2}$	26.50	$n_{m,2}$	18.30
$\beta_{m,3}$	31.15	$\alpha_{m,3}$	34.50	$n_{m,3}$	60.90
$\beta_{m,4}$	46.5	$\alpha_{m,4}$	44.00	$n_{m,4}$	79.00
$\beta_{m,5}$	57.25	$\alpha_{m,5}$	58.50	$n_{m,5}$	103.20
$\beta_{m,6}$	70.70				
$\beta_{m,7}$	94.67				
$\beta_{s,1}$	81.94			$n_{s,1}$	$n_{m,4}+2.94$
$\beta_{s,2}$	79.85			$n_{s,2}$	$n_{m,4}+0.85$
				$n_{s,3}$	$n_{m,1}+16.00$
				$n_{s,4}$	$n_{m,1}+20.00$

Table 3: Location of the environmental quality stations (see Fig. 1). All values are given in km.

	$\gamma_{m,0}$	$\gamma_{m,1}$	$\gamma_{m,2}$	$\gamma_{m,3}$	$\gamma_{m,4}$	$\gamma_{m,5}$	$\gamma_{m,6}$	$\gamma_{m,7}$
km	-5.3	12.0	18.3	20.9	30.0	41.8	52.3	79.0

204 *2.2.3. Data*

205 The GRE was widely monitored during a study carried out between 2008
206 and 2011. The deployed instrumentation is described in detail by Navarro
207 et al. (2011). Among other instruments, tidal gauges, current meters, and
208 environmental quality probes were installed. Figure 1 shows the locations of
209 the equipment employed in this study. Tables 2 and 3 indicate the kilometer
210 points of the instruments' locations. The tidal gauges are denoted by $\beta_{m,i}$ and
211 $\beta_{s,i}$ in Fig. 1. The subscripts are m for locations in the main channel and s for
212 the secondary channels. The hydrodynamic model for the estuary is forced at
213 $x = 0$ km with an M2 tide whose amplitude and phase are determined from
214 sea level data recorded at tidal gauge $\beta_{m,0}$, which is the closest to the mouth
215 in the Port of Bonanza. For this reason, the origin of the along-channel
216 coordinate ($x = 0$ km, positive upstream) is set at this tidal gauge. Another
217 tidal gauge, $\beta_{s,1}$, was situated at the old lock of the Port of Seville, separated
218 from the main channel by a short secondary channel. The tidal gauge denoted
219 as $\beta_{s,2}$ was located 2 km downstream from $\beta_{s,1}$ after the construction of the
220 New Lock, which has allowed access to the Port of Seville since 11/25/2010.
221 Six current meters ($\alpha_{m,i}$ in Fig. 1) were positioned along the main channel
222 between the mouth of the estuary and the Port of Seville. Current data
223 is expressed here in volumetric terms using the tidal prism (e.g. de Jonge,
224 1992; D'Alpaos et al., 2010), which defines the volume of water exchanged in
225 each tidal cycle at each section of the estuary. Eight environmental quality
226 stations or CTDs ($\gamma_{m,i}$ in Fig. 1) provided salinity data. Notice that $\gamma_{m,0}$
227 is located downstream of the Port of Bonanza, i.e., in the negative part of
228 the x-axis. Therefore, to allow for comparing model outputs with salinity

229 observations at that location, both modeled hydrodynamic and salinity data
230 are also shown for $x < 0$.

231 Bathymetric information, which was provided by the Puertos del Estado
232 government agency (State-owned Spanish Port, Ministry of Public Works),
233 was used for calibration of the model. Default values of widths of secondary
234 channels in scenarios 2 and 3 were simply set from distance estimates from
235 Google Earth© historical imagery. Freshwater discharge time-series from the
236 Alcalá del Río Dam, which releases approximately 80% of the total freshwater
237 input into the estuary, were obtained from the Agencia Andaluza del Agua
238 (Regional Water Management Agency). Data about the area and depth of
239 current marshes in the lower part of the estuary were obtained from the
240 Doñana Observatory of Biodiversity and Global Change (information acces-
241 sible from <http://observatorio.ebd.csic.es/>).

242 *2.3. Calibration of the Model in the GRE*

243 Díez-Minguito et al. (2012, 2013) extracted the M2 harmonic constants
244 (amplitudes and phases) from elevation and current data and salinity data,
245 respectively, by using standard harmonic analysis methods (Pawlowicz et al.,
246 2002). The M2 values for the elevation, current, and salinity are shown in
247 Fig. 3. The values of the linearized friction coefficient, r , and the diffusion
248 coefficient, D , for each stretch are obtained by comparing model output with
249 the M2 tidal amplitudes and phases of the elevation and current (symbols in
250 Fig. 3a and Fig. 3b), and the averaged (Fig. 3c) and M2 tidal salinity (Fig. 3c)
251 obtained from the observations. The M2 amplitude of tidal elevations, $a_{M2}^{\hat{\eta}}$,
252 is given as the magnitude of $Z(x)$. The phase of the elevation, $\varphi_{M2}^{\hat{\eta}}$, is the
253 argument of $Z(x)$. Currents and tidal salinity values ($a_{M2}^{\hat{u}}$, $\varphi_{M2}^{\hat{u}}$ and $a_{M2}^{\hat{s}}$) are

254 similarly defined. The methodological details of the calibration process are
255 described in Appendix B.

256 The agreement for amplitudes and phases of elevations (solid red curves in
257 Fig. 3a and Fig. 3b) is good. Determination coefficient values are summarized
258 in Table 4. The R^2 values for the M2 amplitudes and phases are $R^2 = 0.9854$
259 and 0.9973, respectively. The M2 currents, especially the phases, are fairly
260 well described by the model (Fig. 3a and 3b, solid green curves). The fit
261 for M2 amplitudes of tidal currents is poorer than that of tidal elevations,
262 namely, $R^2 = 0.5479$. However, current phases show an excellent agreement
263 ($R^2 = 0.9967$). The best-fit values of the estimated friction coefficients for
264 each stretch are in Table 1. The order of magnitude of the friction coeffi-
265 cient values is $\mathcal{O}(10^{-3})$, similar to that obtained by Álvarez et al. (2001).
266 The greatest values are found close to the mouth of the estuary, where, ac-
267 cording to Díez-Minguito et al. (2012), the effect of the friction on the wave
268 propagation is dominant.

269 The values of averaged salinity $\bar{s}(x)$ and M2 tidal salinity $a_{M2}^{\hat{s}}$ (triangles,
270 Fig. 3c and 3d, respectively) are considered for the fit of the dispersion co-
271 efficient, D . The agreement is once again good (solid blue curves). The
272 determination coefficient for averaged salinity is $R^2 = 0.9967$, and for the
273 amplitude of tidal salinity, 0.9517 is obtained. Best-fit values are shown in
274 Table 1. The dispersion coefficients range between $300 \text{ m}^2/\text{s}$ and $550 \text{ m}^2/\text{s}$ (at
275 the stretch closest to the mouth), decreasing upstream. This value is slightly
276 higher than the most likely value determined by Díez-Minguito et al. (2013),
277 which is $\sim 500 \text{ m}^2/\text{s}$.

Table 4: Determination coefficients R^2 .

$a_{M2}^{\hat{\eta}}$	$\varphi_{M2}^{\hat{\eta}}$	$P_{t,M2}$	$\varphi_{M2}^{\hat{P}t}$	\bar{s}	$a_{M2}^{\hat{s}}$
0.9854	0.9973	0.5479	0.9967	0.9967	0.9517

278 2.4. Description of the Management Scenarios

279 Scenarios 1, 2 and 3 account for the possible management alternatives
 280 that are currently being promoted by different public administrative bodies.
 281 The impacts of the scenarios are evaluated using the calibrated model. Next,
 282 each scenario is described.

283 2.4.1. Scenario 1: Deepening/Shallowing of the Navigation Channel

284 In scenario 1, the effects of the change of the mean depth, h , along the
 285 navigation channel are analyzed. There are currently a number of proposals
 286 regarding the management of the navigation channel of the GRE. On the
 287 one hand, there are proposals to deepen the navigation channel to allow
 288 larger vessels to safely reach the Port of Seville (Ruiz et al., 2015). On the
 289 other hand, there are management proposals which request a reduction in
 290 the amount of maintenance dredging to return, to a certain extent, to a more
 291 natural behavior of the estuary. This would imply larger silting rates within
 292 the estuary, i.e., a reduction in depth. The topology implemented in the
 293 model for this scenario is shown in Fig. 2b. The deepening implemented in
 294 this scenario is modeled as a uniform increase in the mean channel depth
 295 h . A range of values of h between 4 m and 10 m is considered. Notice that,
 296 because cross-sections in the idealized model are rectangular, this scenario
 297 could also replicate the effect of changes in mean sea level.

298 *2.4.2. Scenario 2: The Reconnection of a Secondary Channel (Brazo del*
299 *Oeste)*

300 Historically, shortcuts across meanders were carried out in the GRE to
301 increase the navigability. Secondary tidal channels were closed to restrain
302 saline intrusion. These works caused the loss of various channels of the
303 tidal estuarine network and a deterioration in water quality due to the in-
304 crease in turbidity levels. Scenario 2 (Fig. 2c) consists of the reconnection
305 of the longest secondary tidal channel, the historic Brazo del Oeste (Fig. 1).
306 With an approximate length of 56 km, this secondary channel partially flows
307 throughout the Doñana National Park and intersects with the GRE at two
308 nodes, namely, $n_{m,2}$ at $x = 18.3$ km and node $n_{m,3}$ at $x = 60.9$ km (Fig. 1).
309 The range of widths considered in the experiments for the reconnected chan-
310 nel is set between 100 and 1000 m according to the local topographic restric-
311 tions. The mean depth is maintained at 6.5 m.

312 *2.4.3. Scenario 3: The Recovery of Marshes in the Lower Part of the Estuary*

313 The current proposal to recover marshes in the GRE pursues to reduce
314 the turbidity in the estuary, which is often in a hyperturbid state (Díez-
315 Minguito et al., 2014), and to increase its primary productivity (Ruiz et al.,
316 2017). The recovery of the marshes would favor the increase of the avail-
317 able surface for sediment retention, ebb dominance, and tidal wave friction,
318 further reducing the turbidity in the estuary and mitigating impacts caused
319 by port activities (Caballero et al., 2018). On the other hand, it would also
320 favor the capture of organic and inorganic carbon (e.g. Chmura et al., 2003).
321 Although the along-channel location of the marshes plays a significant role in
322 the hydrodynamics (e.g. Alebregtse et al., 2013), the estuary zone in which

323 the recovery of marshes is proposed is in the lower part of the estuary. This is
 324 the most morphologically and technically viable zone. Consequently, a large
 325 shallow area is added at node $n_{m,1}$, which is located at $x = 12$ km from the
 326 mouth (Fig. 2d, scenario 3). The marshes are idealized as a wide and shallow
 327 secondary channel (stretch $S_{s,5}$) connected to the lower part of the estuary
 328 by transitional stretch ($S_{s,4}$). A depth of 1 m is considered for the marsh
 329 areas, which approximately agrees with other existing marshes in Doñana
 330 National Park. See parameterizations in Table 1. The effect of the recovered
 331 area is analyzed in this scenario (ranging A_r between 25 km^2 and 400 km^2),
 332 as well as the effect of the width of the connection with the main channel
 333 $b_{S_{s,4}}$ (ranging between 0 and 1000 m).

334 **3. Results**

335 *3.1. Scenario 1: Deepening/shallowing of the Navigation Channel*

336 Figure 4 shows the effects of the change in the depth of the main channel
 337 on the M2 tide and salinity. Figure 4a shows the amplitudes of the M2 tidal
 338 elevations along the main channel, $a_{M2}^{\hat{\eta}}$. The current mean depth of the main
 339 channel of the GRE is 6.5 m, and it is marked with a dashed white line. At
 340 this depth, the amplitude of the elevation (Fig. 4a) decreases towards the
 341 head of the estuary in the first kilometers of the lower part of the estuary.
 342 Amplitude stabilizes upstream and finally amplifies again close to the dam
 343 at the head of the estuary, mainly because of the effect of tidal reflection.
 344 Figure 4b shows the M2 tidal prism, P_{tM2} , which is determined at each cross-
 345 section of the estuary. The tidal prism decreases upstream, reaching zero at
 346 the dam. Additionally, both the averaged and M2 amplitudes of the tidal

347 salinity (Fig. 4c and Fig. 4d) decrease upstream, as expected.

348 Channel deepening (i.e., increases in h with respect to the reference value
349 $h = 6.5$ m) produces an increase in both the tidal amplitude of elevations
350 and currents, as is shown in Fig. 3a and Fig. 3b. The increase is not uniform
351 along the channel. Elevations increase more significantly close to the dam,
352 while currents increase more significantly in the lower part of the estuary. For
353 example, the values of $a_{M2}^{\hat{\eta}}$, for $h = 8$ m, are 36% higher than for $h = 6.5$ m.
354 For mean depths larger than $h = 7.8$ m, the amplitude of the elevation does
355 not continue to decrease inside the estuary with respect to the value at its
356 mouth. The amplitude increases upstream monotonically. The deepening of
357 the navigation channel also produces a substantial increase in the M2 current
358 amplitudes. Tidal currents $a_{M2}^{\hat{u}}$ increase along the entire estuary, except for
359 at the head of the estuary. Values are 12% higher for $h = 8$ m than for
360 $h = 6.5$ m.

361 The convergence of the estuary, which is rather weak (Díez-Minguito
362 et al., 2012), is not modified by the uniform change in h along the chan-
363 nel. However, according to Eq. 1b, the channel deepening reduces the drag
364 that the tidal wave experiences, as long as the friction coefficient r is kept
365 constant. Therefore, this friction reduction causes the observed increase in
366 tidal elevations and currents. The friction reduction affects both the incident
367 and reflected wave, whose superposition forms the (total) tidal wave in each
368 stretch. In real conditions, the friction coefficient could even decrease after
369 the deepening due to, for example, the removal of bed forms by dredging,
370 and the increase of salinity and suspended sediment-induced density stratifi-
371 cation (de Jonge et al., 2014). This would further reduce the drag and further

372 increase tidal elevations and amplitudes. On the other hand, a reduction in
373 the mean depth h increases the effect of friction, producing, in turn, a re-
374 duction in tidal elevations and currents (as is shown in Fig. 4a and Fig. 4b,
375 respectively, below the dashed white line). For example, for $h = 4$ m, the
376 reduction would be so significant that the incident tidal energy on the dam
377 would be practically zero.

378 Regarding the effect of the change of depth on salt distribution in the main
379 channel (Fig. 3c), keeping the river flow and the tidal dispersion constant,
380 the deepening of the channel increases the saline intrusion in every case.
381 Deepening also moves the maximum salt gradient upstream. On the other
382 hand, the reduction in the mean depth decreases saline intrusion and moves
383 the maximum salt gradient downstream. Locations of the isohaline 5 are
384 44.6, 39.85 and 26.7 km for depths 8, 6.5 and 4 m, respectively. A deepening
385 of 1 m of the navigation channel increases the average intrusion in the GRE
386 to approximately 3 km, while a reduction of 1 m causes a regression of 5 km.
387 Figure 3d, which represents the M2 amplitude of tidal salinity $a_{M2}^{\hat{s}}$, shows
388 that the greatest amplitudes appear where the salt gradient is higher because
389 the M2 current advects the salinity gradient.

390 *3.2. Scenario 2: The Reconnection of a Secondary Channel (Brazo del Oeste)*

391 Figure 5 shows the effect of the reconnection of the historic Brazo del
392 Oeste on the behavior of the tidal amplitudes and the salinity along the
393 main channel. Figure 6 shows the same properties as Fig. 5, but it is for the
394 tidal amplitudes and salinity along the secondary channel of Brazo del Oeste.
395 The results are shown for different widths of the Brazo del Oeste ($b_{S_s,3}$). In
396 both figures, the dotted white line marks the results for a reference width of

397 the reconnected channel, which is set to 350 m (Table 1).

398 Figure 5a shows the values of the M2 amplitudes of the tidal elevations
399 along the main channel. These are, in general, higher than those observed
400 for the present situation without reconnection. Elevation amplitude attains
401 its maximum at the head of the estuary with a value of 1.7 m for widths
402 of the secondary channel of $b_{\mathbb{S}_{s,3}} \approx 400$ m. Similar behavior is observed
403 for amplitudes of tidal elevations along the Brazo del Oeste (Fig. 6a). The
404 largest amplitudes are observed upstream. This apparently coupled increase
405 of M2 amplitudes both in the main and secondary channel (Fig. 5a and 6a)
406 suggest a connection between both propagated tidal waves. Accordingly, the
407 effect of the variation of the friction coefficient $r_{\mathbb{S}_{s,3}}$ on the elevations has
408 been explored to evaluate the possibility of a resonant behavior. However,
409 preliminary results (not shown) show that in this scenario, for realistic values
410 of the friction coefficient, no resonance is detected for the M2 constituent.
411 Nevertheless, as expected, tidal amplitudes and saline intrusion (given by the
412 distribution of the average salinity) decrease in the entire estuary when the
413 values of the friction coefficient increase.

414 Regarding the tidal prism (Fig. 5b), discontinuities are observed at the
415 connection points of the channels. In general, the tidal prism tends to in-
416 crease from the mouth of the estuary to the seaward connection point at
417 $x \approx 18.30$ km and decreases upstream from that point. In terms of tidal cur-
418 rents, the reconnection of the Brazo del Oeste produces an increase/reduction
419 in the amplitudes of the M2 tidal currents for widths with values lower/higher
420 than 400 m along the GRE from the mouth of the estuary to $x = 20$ km. The
421 highest value of the amplitude $a_{\text{M2}}^{\hat{u}} \sim 1.6$ m/s, is present at approximately

422 $x = 13$ km, downstream from node $n_{m,2}$ and for a width of the Brazo del
423 Oeste $b_{S_s,3} = 1000$ m (Fig. 5b). Along the Brazo del Oeste (Fig. 6b), the val-
424 ues represented for the M2 tidal prism, represented by P_{tM2} , show a decrease
425 upstream because of the effect of friction.

426 The effects of the reconnection of the Brazo del Oeste on the average salin-
427 ity (5c), $\bar{s}(x)$, show a slight increase due to the reduction in river flow, which is
428 distributed between the junction points (at $x = 18.30$ km and $x = 60.90$ km).
429 At these points, both tidal currents (or tidal prisms) and tidal salinity reach
430 their highest values. The most important changes in the amplitudes of tidal
431 salinity also occurred in the first 20 km from the mouth (Fig. 5d). The M2
432 amplitudes of salinity notably decrease close to the mouth of the estuary
433 due to the reduction in M2 tidal currents (Fig. 5b). This indicates that
434 the amplitudes of tidal salinity are largely controlled by the tidal currents.
435 The greatest values of the amplitudes correspond to widths of 100 m, given
436 that the maximum gradient of averaged salinity (Fig. 5c) is found around
437 $x = 15$ km.

438 3.3. Scenario 3: The Recovery of Marshes in the Lower Part of the Estuary

439 The third scenario analyzes the influence of the recovery of marshes in
440 the lower part of the estuary on the behavior of the estuary. The effect of
441 the recovered area Ar and the effect of the width of the transitional stretch
442 between the marshes and the estuary main channel $b_{S_s,4}$, are analyzed.

443 Figure 7 shows the effects on the main channel of the recovery of marshes.
444 In this case, the width of the connecting stretch is kept constant at 60 m. For
445 the range of values in the considered area, both the tidal wave propagation
446 and the salt distribution along the estuary hardly changes. This is shown by

447 the vertical isolines in all of the panels in Fig. 7.

448 However, the larger connection widths $b_{\mathbb{S}_{s,4}}$ have an impact on the hydro-
449 dynamic and transport along the main channel. Figure 8 shows the results
450 for different widths of the transitional stretch $b_{\mathbb{S}_{s,4}}$. Overall, the effects on
451 the dynamics and salinities are noticeable for widths larger than 100 m. The
452 amplitude of the tidal elevations (Fig. 8a) decreases upstream from the con-
453 nection point when the width $b_{\mathbb{S}_{s,4}}$ increases. For instance, for each change
454 in width $\Delta b_{\mathbb{S}_{s,4}} = 50$ m, the amplitude experiences an approximate decrease
455 of $\Delta a_{\hat{\eta}_{M2}} \approx -1$ cm. For the tidal prism (Fig. 8b), its values show that the
456 greater the width of the connection, the larger the values of the tidal prism
457 downstream from the connection point. The tidal prism is reduced upstream
458 with respect to the current situation. The longitudinal distribution of salin-
459 ity (Fig. 8c) is apparently not affected by the presence of marshes. However,
460 the amplitudes of tidal salinity (Fig. 8d) are mainly modified by the change
461 in the amplitudes of the tidal currents that transport the salt field.

462 4. Discussion

463 The results of the experiments carried out with the model provide valu-
464 able information about management alternatives and estuarine dynamics.
465 To streamline the discussion, Fig. 9 shows representative model outputs ob-
466 tained for each scenario (blue curves) compared to the current situation (solid
467 orange curves). Overall, the model results indicate that the channel deepen-
468 ing (scenario 1, solid line) tends to increase the amplitudes of the elevations,
469 the tidal prism, and the saline intrusion in the estuary (Fig. 9a, 9b and 9c,
470 respectively). Similar impacts have been reported in other estuaries (e.g.

471 de Jonge et al., 2014). The reconnection of the secondary channel of the
472 Brazo del Oeste (Scenario 2, dashed line) shows similar effects, except for
473 locations close to the mouth of the estuary, where the amplitudes of the el-
474 evation and tidal currents decrease, including a significant decrease in the
475 latter. Model results for scenario 3 (dotted line) show that along-channel
476 tidal amplitudes and salinity distributions remain almost unmodified when
477 the marshes are connected to the main channel throughout a stretch with
478 a width lower than ~ 100 m. For higher interconnecting widths, the main
479 channel dynamic is affected since a significant part of the tidal momentum
480 is conveyed throughout the marshes.

481 In terms of navigation in the estuary, the higher tidal range values ob-
482 served after a deepening would favor navigation from the mouth of the estu-
483 ary to the Port of Seville. As a matter of fact, vessels follow the high water
484 propagation when navigating over higher depths from the mouth to the Port
485 of Seville. The increase of the tidal range due to dredging must also be
486 therefore considered at a design stage. This effect would allow the volume of
487 dredged material to be optimized (reduced), since lower volumes are required
488 to be dredged to reach a given water column height at high water. On the
489 other hand, considering the notable increase in the tidal amplitudes along
490 the main channel of the estuary observed in scenario 2 (Fig. 9a, dotted blue
491 curve), the reconnection of the Brazo del Oeste could apparently provide an
492 alternative to deepening. For example, dredging the navigation channel to
493 8 m presents similar results for elevations and tidal currents as the connec-
494 tion of the secondary channel of the Brazo del Oeste with $b_{\mathbb{S},3} = 150$ m and
495 $h_{\mathbb{S},3} = 6.5$ m (also with $b_{\mathbb{S},3} = 350$ m and $h_{\mathbb{S},3} = 5$ m).

496 The increase in tidal currents, which is predicted by the model for the
497 deepening scenario (Fig. 9b, Scenario 1), also results in an increase in the
498 shear stress at the bottom. This would increase local erosion rates and the
499 concentration of sediments in suspension. Similar impacts were reported
500 in other nearly well-mixed and turbid estuaries such as the Ems estuary
501 (de Jonge et al., 2014). The increase of tidal currents may thus yield a tur-
502 bidity regime shift that, in the absence of other compensatory measures such
503 as the recovery of tidal marshes (scenario 3), would affect water quality in the
504 estuary, including deteriorated light and oxygen conditions. This was already
505 pointed out by previous studies in the GRE. Ruiz et al. (2013, 2017) indi-
506 cate that photosynthesis is most often inhibited by the turbidity induced by
507 tides, rather than due to catchment-derived sediment inputs. These authors
508 also suggested that further modifications of the GRE, such as increasing its
509 depth for navigation purposes, would have the potential to reduce primary
510 production.

511 The model also quantifies the expected increase in saline intrusion for
512 both a deepening of the channel (Fig. 9c, solid blue curve) and for the recon-
513 nection of the Brazo del Oeste (Fig. 9c, dashed blue curve). The displace-
514 ment of the salinity distribution upstream is more significant in the case of
515 the Brazo del Oeste reconnection, thereby making the control of the salt in-
516 trusion more difficult (e.g., for agricultural activities) and possibly inducing
517 species migration. The increase in the salt intrusion (namely, up to 10 km
518 in the central part of the estuary) is significant with respect to the length
519 of the estuary (~ 110 km). It is also important to highlight that the results
520 were obtained by keeping the longitudinal dispersion and the fresh water flow

521 constant (for low-flow conditions). However, the climatic trend is that, in
522 years to come, fresh water flow will decrease by 15% (Reyes-Merlo et al.,
523 2013). This would make the control of saline intrusion even more compli-
524 cated. Nevertheless, it is expected that, due to the increase in tidal currents,
525 the longitudinal dispersion coefficient would increase, because salinity mix-
526 ing is mainly controlled by tidal action (Díez-Minguito et al., 2013). This
527 change in the mixing time-scale would also reduce the adjustment times of
528 the salinity distribution during tidal-fluvial unsteady regimes.

529 These results suggests that a combination or superposition of manage-
530 ment alternatives could be used to mitigate the specific effects of individual
531 scenarios. For example, the effects of the channel deepening on the am-
532 plitudes of tidal elevations and currents could be partially compensated for
533 by the reconnection of secondary channels or through the recovery and/or
534 creation of marshes. Specifically, Fig. 10 shows how the effects of dredging
535 to 8 m on elevations and currents is mitigated by the reconnection of the
536 Brazo del Oeste (Fig. 10a and 10b, respectively) or by the recovery of the
537 tidal flats in the lower part of the estuary (Fig. 10c and 10d, respectively).
538 The combination of scenarios 1 (channel deepening) and 2 (reconnection of
539 Brazo del Oeste) and scenarios 1 and 3 (recovery of marshes) allow the tidal
540 elevations and currents along the whole estuary to be similar to the current
541 observed values. Obviously, the same is not true for the saline intrusion. A
542 combination of these alternatives would give rise to greater saline intrusion
543 than in the current estuary.

544 Finally, it is noteworthy that the exploratory model is flexible and can
545 be used for drawing general conclusions about tendencies in tide propaga-

546 tion and salinity distribution in response to different management scenarios.
547 However, the model has important limitations. The model does not consider
548 nonlinear effects, which means that it is not able to replicate second order
549 (residual) effects on tidal wave propagation or salt transport. The analysis
550 performed here does not consider any tidal-fluvial interaction effects. The
551 analyses were carried out only for low river flow conditions, during which
552 the effects of tidal-fluvial interactions are negligible in most of the estuary.
553 The determination coefficients obtained comparing, at the calibration stage,
554 model results with tidal elevations and salinity are high. However, model
555 performance decreases when trying to reproduce current observations. Mod-
556 eling currents in estuaries often poses a challenge for even complex numerical
557 models, because currents depend to a larger extent than elevations on topo-
558 graphic and bathymetric complexities.

559 Accordingly, a basic sensitivity analysis is performed over the fitted pa-
560 rameters. These are the friction coefficient r and the effective dispersion
561 coefficient D . Sensitivity is studied using values that vary from half to dou-
562 ble of those considered in each stretch for the reference configuration, namely,
563 $(0.002, 0.0038)$ for r and $(600, 1100) \text{ m}^2/\text{s}$ for D . Fig. 11 shows the relative
564 variations in the amplitudes of tidal elevations for varying r (upper panel)
565 and average salinity with varying D (lower panel). The results indicate that
566 the changes in the outputs of the model are greater if the friction coefficient
567 is modified. Reducing by half (duplicating) the friction coefficient practically
568 duplicates (reduces by half) tidal elevations. In both cases, the greatest de-
569 viations are observed upstream. These results were expected, given that r is
570 a critical parameter in any hydrodynamic model and the effects accumulate

571 as the tidal wave propagates upstream. For the dispersion coefficient, the
572 greatest variations do not reach 50% for the range considered and are only
573 relevant from $x = 80$ km. This analysis suggests that the uncertainty in the
574 predictions, considering the calibrated values of r and D , is below 20%.

575 **5. Conclusions**

576 An exploratory model is used to evaluate and discuss three manage-
577 ment scenarios that are currently being considered by different administrative
578 bodies in the Guadalquivir River Estuary. The one-dimensional linearized
579 shallow-water equations for elevation and currents are solved in stretches.
580 The model expands on previous analytical developments in the determination
581 of the amplitude of tidal salinity along the estuary. The model is calibrated
582 with observations recorded by a monitoring network deployed from 2008 to
583 2011 between the Alcalá del Río head dam and the estuary mouth.

584 Model results suggest that the tidal amplitudes of elevations and currents
585 increase in response to the deepening of the navigational channel. This is due
586 to a reduction in effective friction and an increase in tidal energy reflected at
587 the head dam. The distribution of average salinity moves upstream, increas-
588 ing the saline intrusion, as well as the maximum salinity gradient. The M2
589 tidal salinity, produced by the advection of the averaged salinity gradient,
590 also increases upstream. Opposite effects are observed when the mean water
591 level decreases.

592 The reconnection of the historic secondary channel of Brazo del Oeste,
593 which connects the lower and upper part of the main channel, causes major
594 alterations when compared to the current situation. Tides that propagate

595 through the main and secondary channels interact, thus giving rise to an
596 increase in tidal elevations (especially close to the dam) and currents, except
597 in cross-sections near the mouth of the estuary. For the salt intrusion, the
598 separation of the river flow in the two channels yields the displacement of
599 the salinity distribution upstream.

600 The recovery of marshes in the lower part of the estuary also has notable
601 consequences on the tidal wave propagation. Its effect is more acute when
602 the width of the transitional stretch that connects the marshes with the
603 navigation channel exceeds one hundred meters. The most notable effect is
604 to increase the tidal amplitudes and to reduce the currents upstream from
605 the connection point in proportion to the width of the transitional stretch.

606 From the point of view of management and practitioners, the model allows
607 for an exploration of useful countermeasures for impact mitigation. Model
608 results suggest that the combination of two or more management alterna-
609 tives allows for the mitigation of specific effects of individual scenarios. In
610 particular, the increase of tidal elevations and currents caused by the deep-
611 ening of the navigation channel could be compensated for with the recovery
612 of marshes in the lower part of the estuary.

613 **Acknowledgments**

614 This research was funded by Programa Estatal de I+D+i RETOS (Ref.
615 CTM2017-89531-R) and Fundación Biodiversidad (Ref. PRCV00487). MDM
616 acknowledges support from Spanish public funding programmes: José Castillejo
617 2013-2016 (Ref. CAS17-00247). RSA acknowledges support from CTM2017-
618 89531-R and the Environmental Fluid Dynamics Group (TEP-209). The

619 data in this work can be obtained from Puertos del Estado government agency
620 (<http://www.puertos.es/>), Agencia Andaluza del Agua - Junta de An-
621 dalucía (<http://www.juntadeandalucia.es/>) and ([http://www.chguadalquivir.](http://www.chguadalquivir.es/)
622 [es/](http://www.chguadalquivir.es/)) and TEP-209 (gpyc@ugr.es). The authors would like to thank the two
623 anonymous reviewers and Prof. Victor N. de Jonge (Editor in Chief) for
624 their valuable comments and suggestions, which have greatly contributed to
625 improve this work.

626 **Appendix A. Procedure for the Calculation of Elevations, Cur-**
627 **rents and Salinity**

628 Figure A.12 shows the procedure used to calculate all of the variables.
629 Once the values of r and D of the model adjustment (step 1) are obtained, the
630 tidal elevations and currents are calculated, $\hat{\eta}$ and \hat{u} , using the derived Eqs. 5
631 (step 2). Because the cross-sections of each stretch are known, b and h , \hat{Q} ,
632 and the tidal prism, P_t , can also be deduced. The following step is to get the
633 mean components. Starting from the combination of Eqs. 1-3, the following
634 system is deduced for the averaged variables: $\partial\bar{\eta}/\partial x + r\bar{u}/h = 0$, $\partial\bar{u}/\partial x = 0$
635 and $\partial\bar{s}/\partial x = D\partial^2\bar{s}/\partial x^2$. Solving this system allows the Eq. A.1 for the
636 averaged elevations, $\bar{\eta}$, to be obtained for each stretch (step 3). Similarly,
637 Eq. A.2 for averaged flows and currents \bar{Q} and \bar{u} , (step 4) and the average
638 salinity, \bar{s} , with Eq. A.3 (step 5), are obtained as follows (Prandle, 1981):

$$\bar{\eta}(x) = -\frac{f Q_d}{g h b T_{M2} \sqrt{g h}} x + d, \quad (\text{A.1})$$

$$\bar{u}(x) = Q_d/(bh), \quad (\text{A.2})$$

$$\bar{s}(x) = \delta_2 \exp \lambda x + \delta_1/\lambda, \quad (\text{A.3})$$

639 Here, d , δ_1 and δ_2 are constants determined by imposing the boundary
640 conditions (and the matching conditions in the case of intermediate nodes),
641 Q_d is the fresh water discharge, and f is an effective friction coefficient at
642 the averaged scale. For this application in the Guadalquivir estuary, the
643 discharge is assumed to be a constant $40 \text{ m}^3/\text{s}$, as in a low river-flow regime.

$$\hat{s}(x) = x\hat{A} \exp((i\kappa + \lambda)x) - x\hat{B} \exp(-(i\kappa - \lambda)x) \quad (\text{A.4})$$

644 Coefficients \hat{A} and \hat{B} are equal to the following:

$$\hat{A} = \frac{A\sigma\lambda\delta_2/(\kappa h)}{D(i\kappa + \lambda)(2 + (i\kappa + \lambda)x) - (\bar{u}(1 + (i\kappa + \lambda))x) - (i\sigma x)}, \quad (\text{A.5a})$$

645

$$\hat{B} = \frac{B\sigma\lambda\delta_2/(\kappa h)}{-D(i\kappa - \lambda)(2 - (i\kappa - \lambda)x) - (\bar{u}(1 - (i\kappa - \lambda))x) - (i\sigma x)}, \quad (\text{A.5b})$$

646 with $\lambda = Q_d/(bhD)$.

647 Additionally, the method of superposition of solutions by Lugt (2012),
 648 which is a perturbative method, was also used to verify that the model results
 649 of the reference case determined with the procedure described are correct.
 650 For both methods, differences at all locations are within the error bars of the
 651 tidal constants determined from observations. The greatest discrepancies
 652 are produced around node $n_{m,4}$, which connects the main channel with the
 653 entrance to the Port of Seville.

654 **Appendix B. Calibration of the Model: Friction and Dispersion** 655 **Coefficients**

656 The data observed and employed for the calibration of the model were
 657 recorded by the monitoring campaign carried out between 2008 and 2011.
 658 The configuration of the GRE during the campaign comprises six stretches
 659 $\mathbb{S}_{m,1}$, $\mathbb{S}_{m,2}$, $\mathbb{S}_{m,3}$, $\mathbb{S}_{m,4}$, $\mathbb{S}_{m,5}$ and $\mathbb{S}_{s,1}$ (see Fig. 2a).

660 The adjustment of the model was carried out by obtaining the values
 661 of the linearized friction coefficient r , and the diffusion coefficient, D , for
 662 each stretch. For this purpose, Eqs. 5 and 7 were applied. The system of
 663 equations has twelve unknowns, two for each stretch, and requires twelve

664 boundary and matching conditions (for both elevations and currents) to be
 665 solved. For the calculation of r , the conditions are as follows:

$$\begin{aligned}
 \hat{\eta}_{\mathbb{S}_{m,1}}(n_{m,0}, t) &= a_0^{\hat{\eta}}, & (\text{B.1}) \\
 \hat{u}_{\mathbb{S}_{m,5}}(n_{m,5}, t) &= \hat{u}_{\mathbb{S}_{s,1}}(n_{s,1}, t) = 0, \\
 \hat{\eta}_{\mathbb{S}_{m,k}}(n_{m,k}, t) &= \hat{\eta}_{\mathbb{S}_{m,k+1}}(n_{m,k}, t), \\
 &\text{for } k = 1, \dots, 4. \\
 \hat{\eta}_{\mathbb{S}_{m,4}}(n_{m,4}, t) &= \hat{\eta}_{\mathbb{S}_{s,1}}(n_{m,4}, t), \\
 \hat{u}_{\mathbb{S}_{m,k}}(n_{m,k}, t) b_{m,k} h_{m,k} &= \hat{u}_{\mathbb{S}_{m,k}}(n_{m,k}, t) b_{m,k+1} h_{m,k+1}, \\
 &\text{for } k = 1, 2, 3. \\
 \hat{u}_{\mathbb{S}_{m,4}}(n_{m,4}, t) b_{m,4} h_{m,4} + \hat{u}_{\mathbb{S}_{s,1}}(n_{m,4}, t) b_{s,1} h_{s,1} &= \\
 \hat{u}_{\mathbb{S}_{m,5}}(n_{m,4}, t) b_{m,5} h_{m,5} &
 \end{aligned}$$

666 where $a_0^{\hat{\eta}}$ is the value of the amplitude of tidal elevation for the constituent
 667 given at node $n_{m,0}$. The amplitude of tidal elevations for the M2 harmonic is
 668 defined as $a_{\text{M2}}^{\hat{\eta}}$, the phase of the tidal elevations for the M2 harmonic as $\varphi_{\text{M2}}^{\hat{\eta}}$,
 669 and similarly for \hat{u} , \hat{Q} and \hat{s} . With these conditions, the dependent variables
 670 for each stretch, i.e., the complex amplitudes of the incident and reflected
 671 wave, can be expressed using the vector $\mathbb{X} = [A_{\mathbb{S}_{m,1}}, B_{\mathbb{S}_{m,1}}, A_{\mathbb{S}_{m,2}}, B_{\mathbb{S}_{m,2}}, A_{\mathbb{S}_{m,3}},$
 672 $B_{\mathbb{S}_{m,3}}, A_{\mathbb{S}_{m,4}}, B_{\mathbb{S}_{m,4}}, A_{\mathbb{S}_{m,5}}, B_{\mathbb{S}_{m,5}}, A_{\mathbb{S}_{s,1}}, B_{\mathbb{S}_{s,1}}]$, and results such as $\mathbb{A} \cdot \mathbb{X} = \mathbb{B}$,
 673 where, $\mathbb{B} = [a_0^{\hat{\eta}}, 0, 0, 0, 0, 0, 0, 0, 0, 0, 0, 0]$, and $\mathbb{A} = (\partial_{i,j})_{12 \times 12}$.

674 The rows in \mathbb{A} correspond with the boundary and matching conditions
 675 and are ordered in the same way as the list of Eq. B.1. The stretches $\mathbb{S}_{m,1}$,
 676 $\mathbb{S}_{m,2}$, $\mathbb{S}_{m,3}$, $\mathbb{S}_{m,4}$, $\mathbb{S}_{m,5}$ and $\mathbb{S}_{s,1}$ correspond to the columns of the matrix \mathbb{A} ,
 677 established for each stretch. The fit is obtained by comparing the observed

678 and modeled values of $\bar{\eta}(x)$. Values of r that are assigned for each stretch
 679 correspond to the values that comply with the condition of a minimum dis-
 680 tance between each curve. In Fig. 3 the results of the adjustment are shown.
 681 The matching and boundary conditions for the averaged elevations, $\bar{\eta}$, are
 682 set to obtain the mean flow, \bar{Q} . These conditions are as follows:

$$\begin{aligned}
 Q_d &= \bar{Q}_{\mathbb{S}_{m,k}} \text{ for } k = 1, \dots, 5. & (\text{B.2}) \\
 \bar{Q}_{\mathbb{S}_{s,1}} &= 0, \\
 \bar{\eta}_{\mathbb{S}_{m,1}}(n_{m,\gamma_0}) &= 0, \\
 \bar{\eta}_{\mathbb{S}_{m,k}}(n_{m,k}) &= \bar{\eta}_{\mathbb{S}_{m,k+1}}(n_{m,k}) \text{ for } k = 1, \dots, 4. \\
 \bar{\eta}_{\mathbb{S}_{s,1}} &= \bar{\eta}_{\mathbb{S}_{m,4}}(n_{m,4}) = \text{const}.
 \end{aligned}$$

683 These conditions set twelve linearly independent equations, and thus
 684 twelve unknowns are determined, which are defined as $\bar{Q}_{\mathbb{S}_{m,1}}$, $\bar{Q}_{\mathbb{S}_{m,2}}$, $\bar{Q}_{\mathbb{S}_{m,3}}$,
 685 $\bar{Q}_{\mathbb{S}_{m,4}}$, $\bar{Q}_{\mathbb{S}_{m,5}}$, $\bar{Q}_{\mathbb{S}_{s,1}}$, $\bar{\eta}_{\mathbb{S}_{m,1}}$, $\bar{\eta}_{\mathbb{S}_{m,2}}$, $\bar{\eta}_{\mathbb{S}_{m,3}}$, $\bar{\eta}_{\mathbb{S}_{m,4}}$, $\bar{\eta}_{\mathbb{S}_{m,5}}$ and $\bar{\eta}_{\mathbb{S}_{s,1}}$. Similarly, the fol-
 686 lowing equations can be solved, and the average salinity, \bar{s} , can be obtained
 687 for each stretch. These are as follows:

$$\begin{aligned}
 \bar{s}_{\mathbb{S}_{m,1}}(n_{m,\gamma_{m,0}}) &= \bar{s}_0, \text{ and } \bar{s}_{\mathbb{S}_{m,5}}(n_{m,5}) = \bar{s}_L = 0, & (\text{B.3}) \\
 \bar{s}_{\mathbb{S}_{m,k}}(n_{m,k}) &= \bar{s}_{\mathbb{S}_{m,k+1}}(n_{m,k}), \text{ for } k = 1, \dots, 4, \\
 \frac{d\bar{s}_{\mathbb{S}_{m,k}}(n_{m,k})}{dx} &= \frac{d\bar{s}_{\mathbb{S}_{m,k+1}}(n_{m,k})}{dx}, \text{ for } k = 1, \dots, 4.
 \end{aligned}$$

688 where \bar{s}_0 and \bar{s}_L are the observed values of the average salinity at the mouth
 689 and the head of the estuary, respectively. No fresh water discharge is consid-

690 ered in any secondary channel. Equation A.4 is used to calculate the tidal
691 salinity, \hat{s} . In this case, the boundary conditions at the mouth and the head
692 are, respectively, $\hat{s}_{\mathbb{S}_{m,1}}(n_{m,\gamma_{m,0}}) = \hat{s}_0$ and $\hat{s}_{\mathbb{S}_{m,5}}(n_{m,5}) = \hat{s}_L = 0$.

693 Finally, to verify that the estimates of the friction coefficient for each
694 stretch are appropriate, the reference configuration is modeled with the same
695 values. The difference between the configuration during the field campaign
696 (2008-2011) and the reference configuration (current situation) is in the di-
697 mensions of the secondary channel (see Fig. 2a and 2b). The construction
698 of the New Lock meant shortening of the secondary channel of the Port of
699 Seville by approximately two kilometers from that of the configuration dur-
700 ing the field campaign. After the construction, the modeled amplitudes of
701 tidal elevations for the M2 harmonic, $a_{\text{M2}}^{\hat{\eta}}$, increased by ~ 3 cm at the con-
702 nection with the main channel. This agrees with the ~ 2 cm M2 amplitude
703 of elevations determined by standard harmonic analysis from the sea level
704 data registered by the Puertos del Estado government agency.

705 Beyond the agreement between model and observations, the construction
706 of the New Lock meant mostly local influence on the dynamics. Assuming
707 that the reference mean level is located at the Port of Bonanza, i.e., $\bar{\eta}(n_{m,0}) =$
708 0 m, the averaged elevation in the Port of Seville is $\bar{\eta}(n_{m,4}) = 0.36$ m (Losada
709 et al., 2017). This value allows the friction coefficient to be estimated at the
710 averaged scale from Eq. A.1, which gives a value of $f \approx 600$ m/s.

711 **References**

712 Alebregtse, N. C., de Swart, H. E., and Schuttelaars, H. M. (2013). Resonance
713 characteristics of tides in branching channels. *Journal of Fluid Mechanics*,

714 728:R3.

715 Álvarez, O., Tejedor, B., and Vidal, J. (2001). La dinámica de marea en
716 el estuario del Guadalquivir: un caso peculiar de *resonancia antrópica*.
717 *Física la Tierra*, pages 11–24.

718 Caballero, I., Navarro, G., and Ruiz, J. (2018). Multi-platform assessment of
719 turbidity plumes during dredging operations in a major estuarine system.
720 *International Journal of Applied Earth Observation and Geoinformation*,
721 68:31–41.

722 Cai, H., Savenije, H. H. G., and Toffolon, M. (2012). A new analytical
723 framework for assessing the effect of sea-level rise and dredging on tidal
724 damping in estuaries. *Journal of Geophysical Research: Oceans*, 117(03).

725 Cai, H., Toffolon, M., and Savenije, H. H. G. (2016). An analytical approach
726 to determining resonance in semi-closed convergent tidal channels. *Coastal*
727 *Engineering Journal*, 58(03):1650009.

728 Chmura, G. L., Anisfeld, S. C., Cahoon, D. R., and Lynch, J. C. (2003).
729 Global carbon sequestration in tidal, saline wetland soils. *Global Biogeo-*
730 *chemical Cycles*, 17(4).

731 Clark, J. R. (1997). Coastal zone management for the new century. *Ocean*
732 *& Coastal Management*, 37(4):191–216.

733 Contreras, D. G. (2009). Estuario del río Guadalquivir: tramificación,
734 pérdidas de carga y modelo lineal de propagación de onda de marea. M.Sc.
735 Thesis. University of Granada.

- 736 D'Alpaos, A., Lanzoni, S., Marani, M., and Rinaldo, A. (2010). On the
737 tidal prism–channel area relations. *Journal of Geophysical Research: Earth*
738 *Surface*, 115(F1).
- 739 de Jonge, V. (1992). Tidal flow and residual flow in the Ems estuary. *Estu-*
740 *arine, Coastal and Shelf Science*, 34(1):1–22.
- 741 de Jonge, V. N., Schuttelaars, H. M., van Beusekom, J. E., Talke, S. A.,
742 and de Swart, H. E. (2014). The influence of channel deepening on estu-
743 arine turbidity levels and dynamics, as exemplified by the Ems estuary.
744 *Estuarine, Coastal and Shelf Science*, 139:46–59.
- 745 del Moral Ituarte, L. (1991). *La obra hidráulica en la Cuenca Baja del*
746 *Guadalquivir, siglos XVIII-XX: gestión del agua and organización del ter-*
747 *ritorio*, volume 3. Universidad de Sevilla.
- 748 Díez-Minguito, M., Baquerizo, A., Ortega-Sánchez, M., Navarro, G., and
749 Losada, M. Á. (2012). Tide transformation in the Guadalquivir estuary
750 (SW Spain) and process-based zonation. *Journal of Geophysical Research:*
751 *Oceans (1978–2012)*, 117(C3).
- 752 Díez-Minguito, M., Contreras, E., Polo, M., and Losada, M. Á. (2013).
753 Spatio-temporal distribution, along-channel transport, and post-riverflood
754 recovery of salinity in the Guadalquivir estuary (SW Spain). *Journal of*
755 *Geophysical Research: Oceans*, 118(5):2267–2278.
- 756 Díez-Minguito, M., Baquerizo, A., de Swart, H., and Losada, M. Á. (2014).
757 Structure of the turbidity field in the Guadalquivir estuary: Analysis of

- 758 observations and a box model approach. *Journal of Geophysical Research:*
759 *Oceans*, 119(10):7190–7204.
- 760 Garel, E. and Cai, H. (2018). Effects of Tidal-Forcing Variations on Tidal
761 Properties Along a Narrow Convergent Estuary. *Estuaries and Coasts*,
762 pages 1–19.
- 763 Geyer, W. R. and MacCready, P. (2014). The estuarine circulation. *Annual*
764 *Review of Fluid Mechanics*, 46.
- 765 González Arteaga, J. M. et al. (1993). Valencianos and arroz en las marismas
766 del Guadalquivir. *Revista de Estudios Andaluces*, (19):67–95.
- 767 Hill, A. and Souza, A. (2006). Tidal dynamics in channels: 2. Complex
768 channel networks. *Journal of Geophysical Research: Oceans (1978–2012)*,
769 111(C11).
- 770 Ianniello, J. (1977). Tidally induced residual currents in estuaries of constant
771 breadth and depth. *Journal of Marine Research*, 35:755–786.
- 772 Li, C., Schuttelaars, H. M., Roos, P. C., Damveld, J. H., Gong, W., and
773 Hulscher, S. J. (2016). Influence of retention basins on tidal dynamics in
774 estuaries: Application to the Ems estuary. *Ocean & Coastal Management*,
775 134:216–225.
- 776 Losada, M. Á., Díez-Minguito, M., and Reyes-Merlo, M. (2017). Tidal-fluvial
777 interaction in the Guadalquivir River Estuary: Spatial and frequency-
778 dependent response of currents and water levels. *Journal of Geophysical*
779 *Research: Oceans*, 122(2):847–865.

- 780 Lugt., D. (2012). The Influence of Retention Basins on Tidal Dynamics in
781 Estuaries. Bachelor of Science in Applied Mathematics. Delft University
782 of Technology..
- 783 Navarro, G., Gutierrez, F. J., Díez-Minguito, M., Losada, M. Á., and Ruiz,
784 J. (2011). Temporal and spatial variability in the Guadalquivir Estuary:
785 A challenge for real-time telemetry. *Ocean Dynamics*, 61(6):753–765.
- 786 Officer, C. B. (1976). Physical oceanography of estuaries and associated
787 coastal waters. In *Physical oceanography of estuaries and associated coastal*
788 *waters*. John Wiley.
- 789 Pawlowicz, R., Beardsley, B., and Lentz, S. (2002). Classical tidal harmonic
790 analysis including error estimates in MATLAB using T-TIDE. *Computers*
791 *& Geosciences*, 28:929–937.
- 792 Prandle, D. (1981). Salinity Intrusion in Estuaries. *Journal of Physical*
793 *Oceanography*, 11:1311–1324.
- 794 Prandle, D. and Rahman, M. (1980). Tidal response in estuaries. *Journal of*
795 *Physical Oceanography*, 10(10):1552–1573.
- 796 Reyes-Merlo, M. Á., Díez-Minguito, M., Ortega-Sánchez, M., Baquerizo, A.,
797 and Losada, M. Á. (2013). On the relative influence of climate forcing
798 agents on the saline intrusion in a well-mixed estuary: Medium-term Monte
799 Carlo predictions. *Journal of Coastal Research*, 65(sp2):1200–1205.
- 800 Ruiz, J., Macías, D., Losada, M. Á., Díez-Minguito, M., and Prieto, L.
801 (2013). A simple biogeochemical model for estuaries with high sediment

802 loads: Application to the Guadalquivir River (SW Iberia). *Ecological mod-*
803 *elling*, 265:194–206.

804 Ruiz, J., Polo, M., Díez-Minguito, M., Navarro, G., Morris, E., Huertas, E.,
805 Caballero, I., Contreras, E., and Losada, M. Á. (2015). The Guadalquivir
806 estuary: A hot spot for environmental and human conflicts. In Finkl, C. W.
807 and Makowski, C., editors, *Environmental Management and Governance*,
808 volume 8 of *Coastal Research Library*, pages 199–232. Springer.

809 Ruiz, J., Macías, D., and Navarro, G. (2017). Natural forcings on a
810 transformed territory overshoot thresholds of primary productivity in the
811 Guadalquivir estuary. *Continental Shelf Research*, 148:199–207.

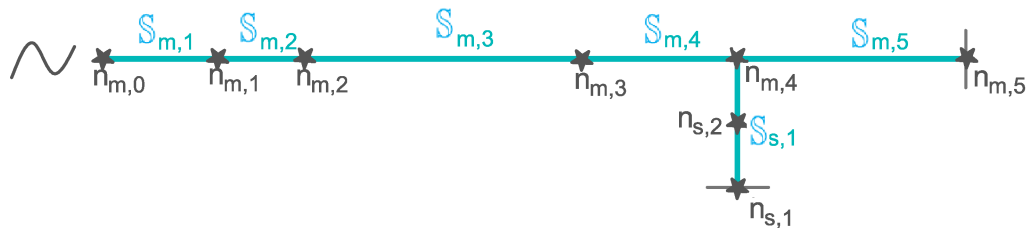
812 Schuttelaars, H. M., de Jonge, V. N., and Chernetsky, A. (2013). Improving
813 the predictive power when modelling physical effects of human interven-
814 tions in estuarine systems. *Ocean & coastal management*, 79:70–82.

815 Souza, A. and Hill, A. (2006). Tidal dynamics in channels: Single channels.
816 *Journal of Geophysical Research: Oceans (1978–2012)*, 111(C9).

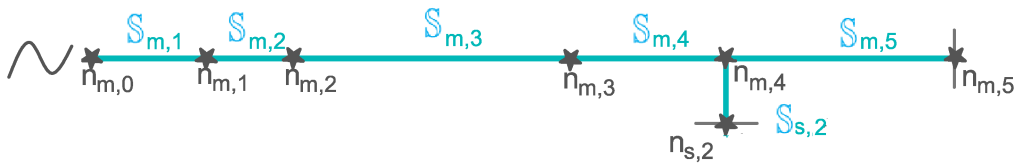
817 Stepanova, O. (2015). Conflict resolution in coastal resource management:
818 Comparative analysis of case studies from four European countries. *Ocean*
819 *& Coastal Management*, 103:109–122.

820 van Maren, D. S., van Kessel, T., Cronin, K., and Sittoni, L. (2015). The
821 impact of channel deepening and dredging on estuarine sediment concen-
822 tration. *Continental Shelf Research*, 95:1–14.

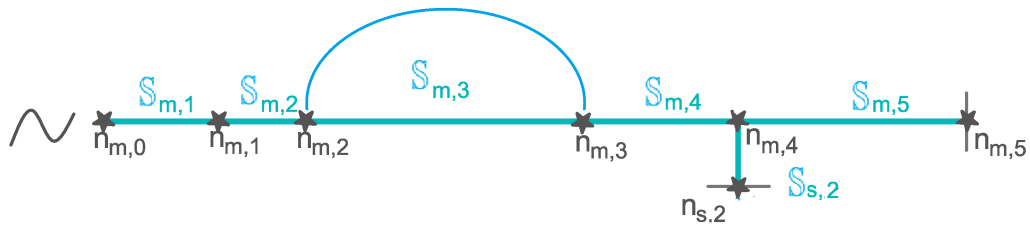
- 823 van Rijn, L. C. (2011). Analytical and numerical analysis of tides and salin-
824 ities in estuaries; part I: tidal wave propagation in convergent estuaries.
825 *Ocean Dynamics*, 61(11):1719–1741.
- 826 Wong, K.-C. (1991). The response of the Delaware estuary to the combined
827 forcing from Chesapeake bay and the ocean. *Journal of Geophysical Re-*
828 *search: Oceans (1978–2012)*, 96(C5):8797–8809.
- 829 Zarzuelo, C., López-Ruiz, A., D’Alpaos, A., Carniello, L., and Ortega-
830 Sánchez, M. (2018). Assessing the morphodynamic response of human-
831 altered tidal embayments. *Geomorphology*, 320:127–141.



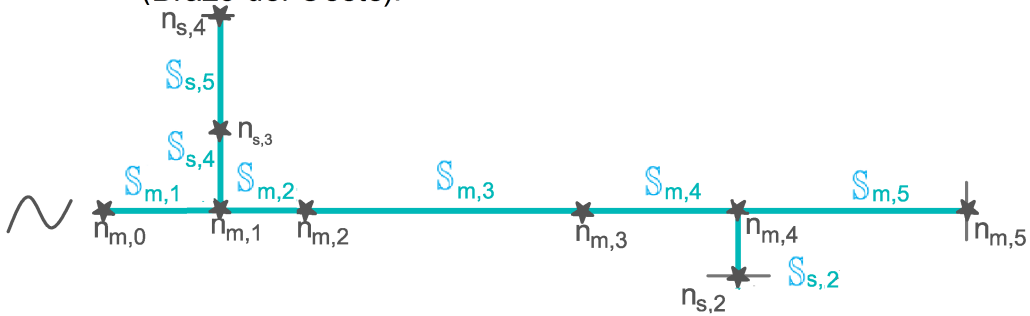
(a) Configuration 2008-2011 for calibration.



(b) Current situation and Scenario 1: Deepening/Shallowing of the Navigation Channel.



(c) Scenario 2: The Reconnection of a Secondary Channel (Brazo del Oeste).



(d) Scenario 3: The Recovery of Marshes in the Lower Part of the Estuary.

Figure 2: Topological representation of the estuary. Panel (a): topology employed for the calibration of the model and the fitting of parameters r and D at each stretch. Panels (b), (c), and (d) show the topology of the different alternatives (or Scenarios 1, 2 and 3), respectively. The following symbols are common to all the cases: nodes are denoted with \star ($n_{i,j}$, with $i=m, s$ and $j=0, \dots, 6$), stretches with blue lines ($S_{i,j}$, with $i = m, s$ and $j = 0, \dots, 6$), barrier with $|$, and M2 tidal forcing at the mouth with \sim . The real locations of the nodes are shown in Fig. 1.

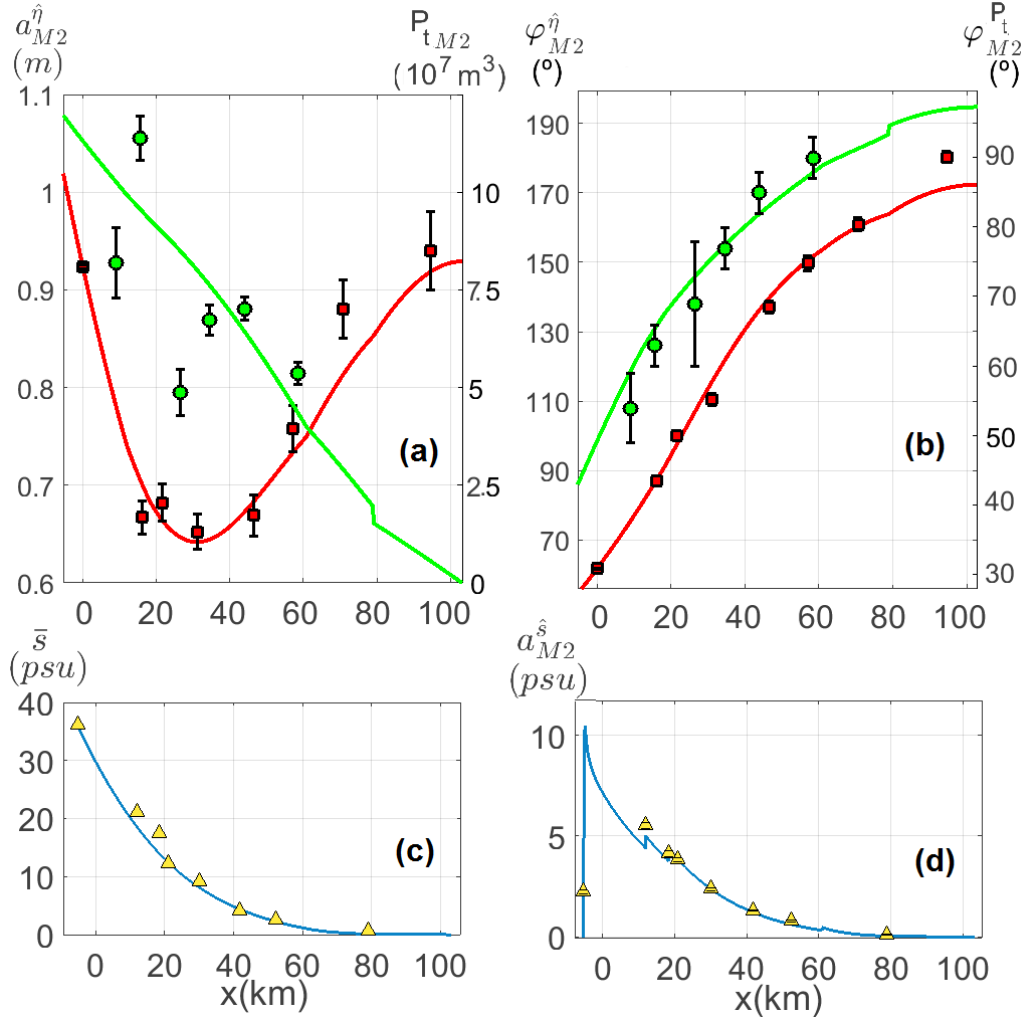


Figure 3: Results of the calibration of the model. Solid lines show the results of the model and the symbols show the tidal data observed for the constituent M2. Panel (a): amplitudes of tidal elevation (curves and red symbols), $a_{M2}^{\hat{\eta}}$, and tidal prism (in green), P_{tM2} . Panel (b): tidal elevation phase (curves and red symbols) $\varphi_{M2}^{\hat{\eta}}$, and tidal current phase (in green) $\varphi_{M2}^{\hat{P}_t}$. Panel (c): averaged salinity, $\bar{s}(x)$. Panel (d): M2 amplitude of the tidal salinity, $a_{M2}^{\hat{s}}(x)$.

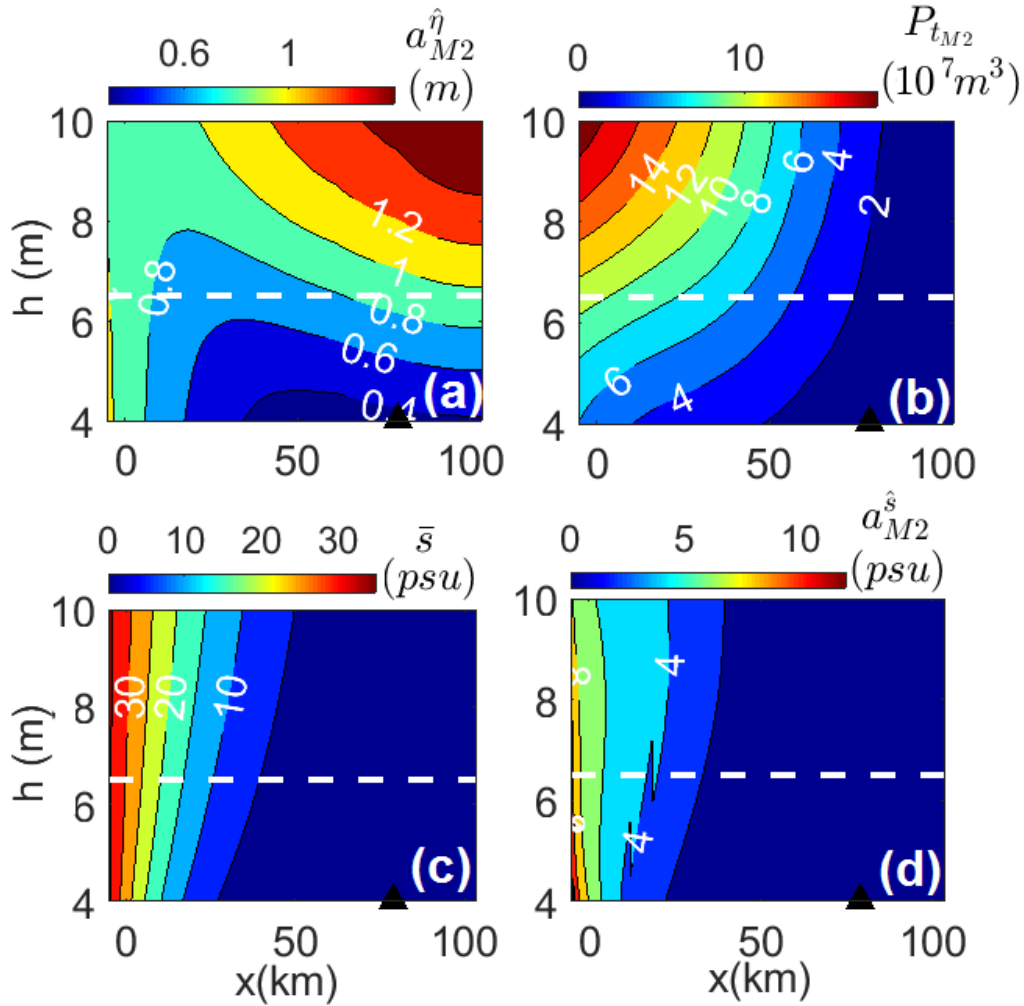


Figure 4: Scenario 1: Results associated with the change in mean depth in the main channel, including color plots of the amplitudes of the M2 tidal elevations (panel (a)), M2 tidal prism (panel (b)), averaged salinity (panel (c)), and the M2 amplitude of tidal salinity (panel (d)) along the main channel for different depths h (y-axis). The x-axis represents distance to the estuary mouth. The location of the secondary channel of the Port of Seville is denoted by \blacktriangle . The dashed white line represents the current mean depth of the estuary, 6.5 m.

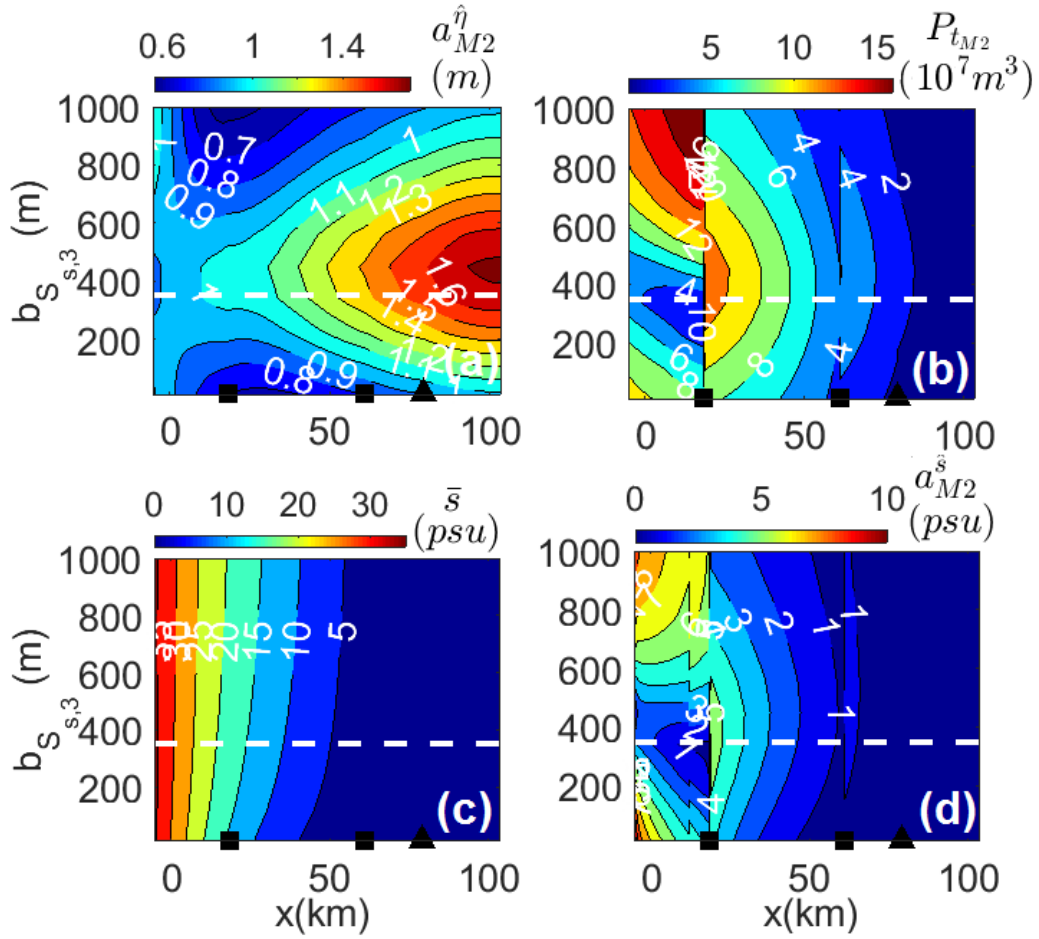


Figure 5: Scenario 2: Results along the main channel after the reconnection of the Brazo del Oeste, including color plots of the M2 amplitudes of the tidal elevations (panel (a)), M2 tidal prism (panel (b)), average salinity (panel (c)) and the M2 amplitude of the tidal salinity (panel (d)) as a function of the width of the Brazo del Oeste, $b_{S,s,3}$. The dashed white line represents the default width of 350 m. The connection points of the Brazo del Oeste at $x = 18.3$ km and $x = 60.9$ km are marked with \blacksquare , whereas the location of the Port of Seville is identified with \blacktriangle .

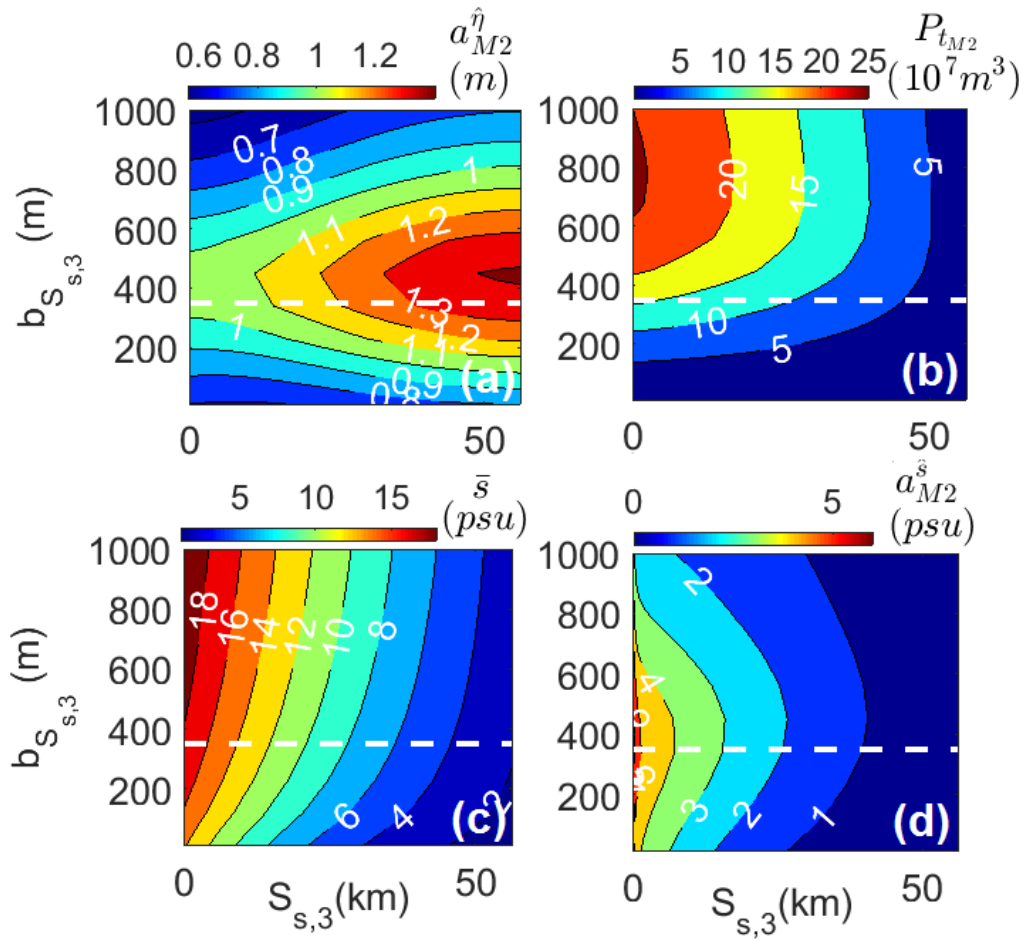


Figure 6: Scenario 2: Results along the secondary tidal channel of the Brazo del Oeste. The panels show the same variables as in Fig. 5. Here, km 0 represents the seaward junction point with the main channel downstream (node $n_{m,2}$).

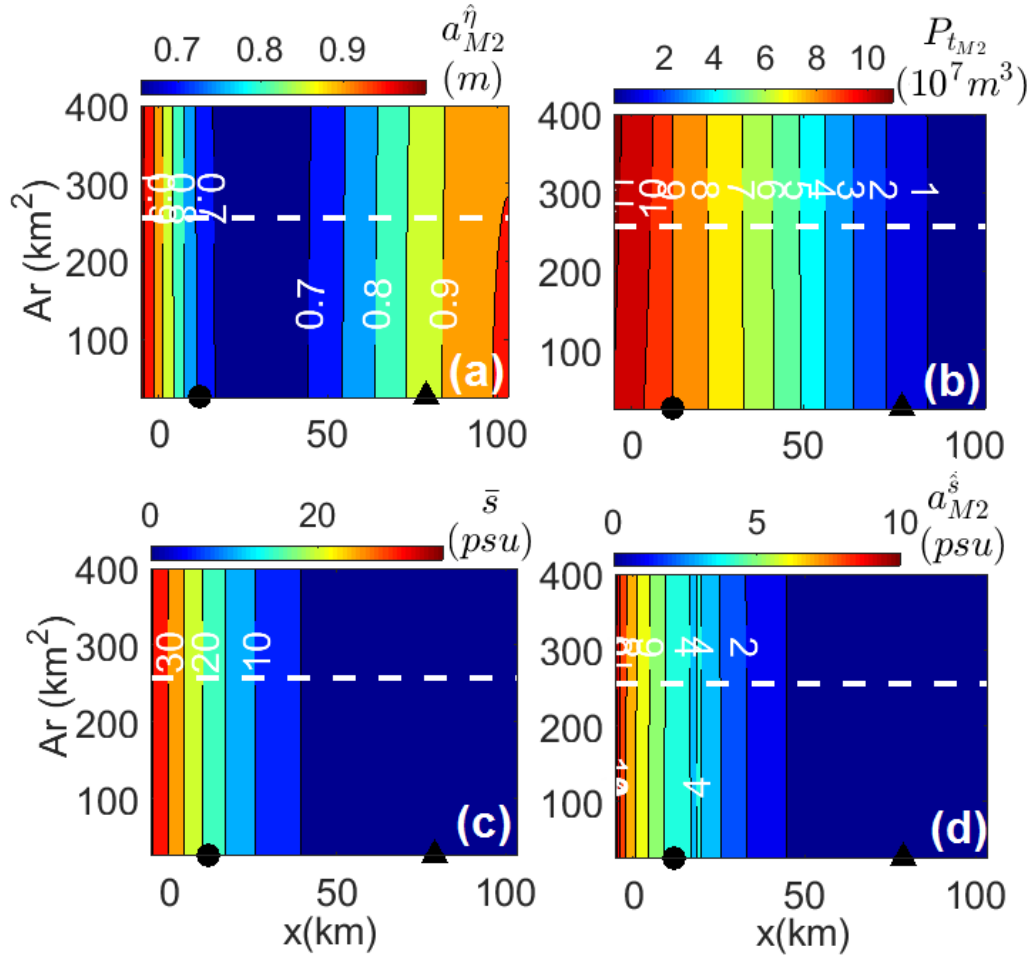


Figure 7: Scenario 3: Results along the main channel associated with the recovery of marshes in the lower part of the estuary, including color plots of the M2 amplitudes of tidal elevations (panel (a)), M2 tidal prism (panel (b)), average salinity (panel (c)) and the M2 amplitude of the tidal salinity (panel (d)) for different values of the total marsh area Ar . The locations of the connection of the marshes with the estuary and the Port of Seville are denoted in the panels by \bullet and \blacktriangle , respectively. The dashed white line corresponds to the default parameters indicated in Table 1. In particular, the width of the first connected stretch $b_{S_s,4}$ is 60 m.

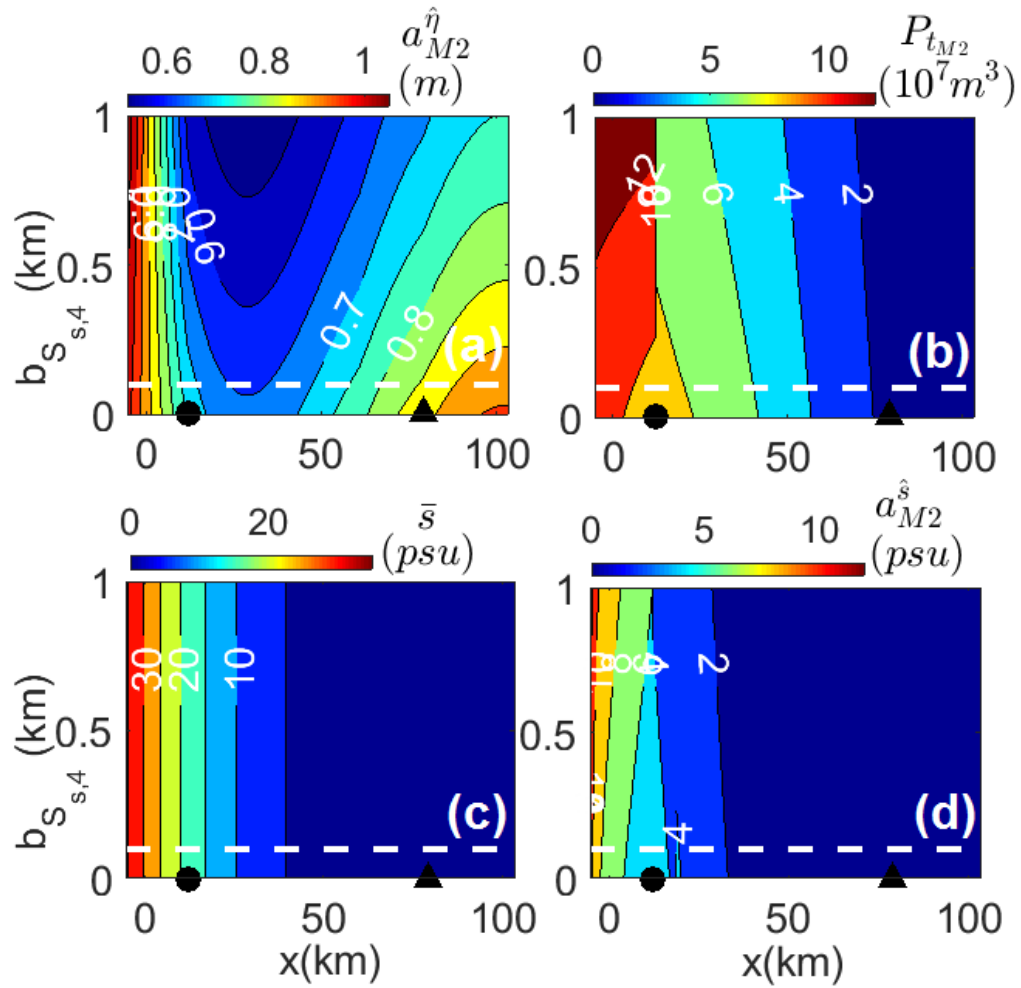


Figure 8: Scenario 3 (recovery of tidal marshes). This figure shows the same variables as in Fig. 7 but with width variations in the first connected stretch, $b_{s,s,4}$ (vertical y-axis).

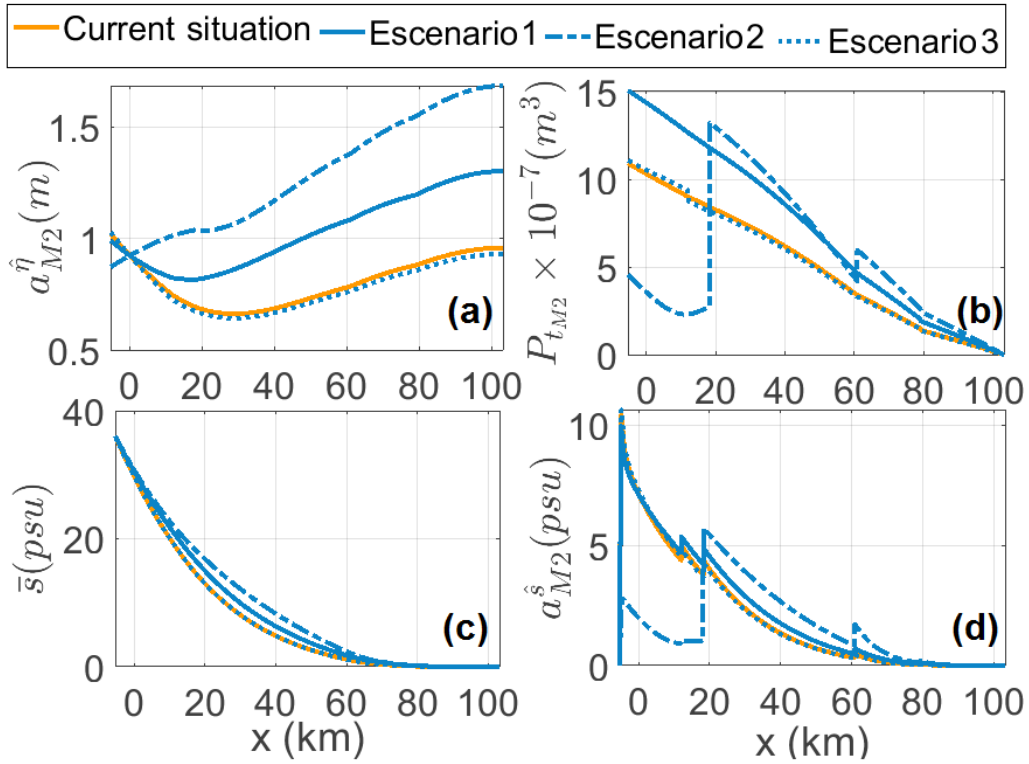


Figure 9: Selection of results along the main channel for the different Scenarios. Panel (a): M2 amplitudes of tidal elevations. Panel (b): M2 tidal prism. Panel (c): average salinity. Panel (d): M2 amplitudes of tidal salinity. Solid orange curves show the current situation in the GRE. Solid blue curves correspond to scenario 1 (channel deepening) for $h = 8$ m. Dashed blue curves correspond to scenario 2 (reconnection of secondary channel of the Brazo del Oeste) for a width of 350 m and a mean depth of 6.5 m. Dotted blue curves correspond to scenario 3 (recovery of marshes) for a width of the connecting stretch with the channel of 60 m.

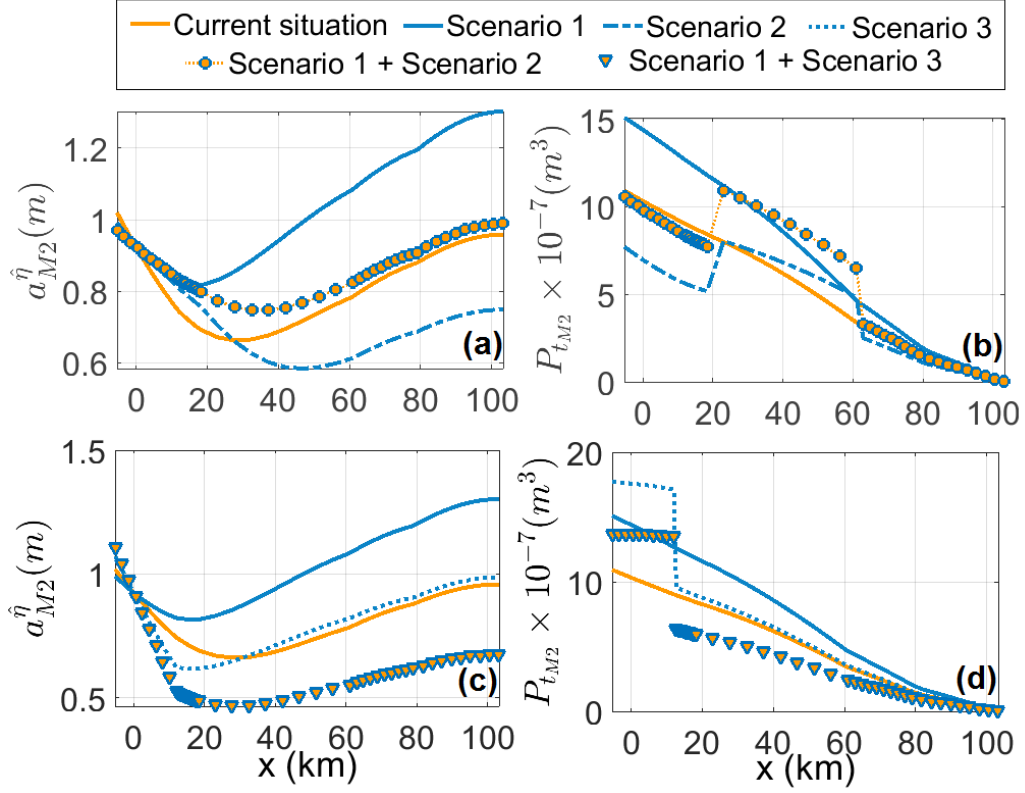


Figure 10: Mitigation of the effects induced on tidal amplitudes and currents due to a channel deepening of $h = 8$ m. Mitigation is performed through the reconnection of the Brazo del Oeste with a mean depth of $h_{S_{s,3}} = 2$ m (panels (a) and (b)) or through the recovery of marshes with mean depth $h_{S_{s,4}} = 2$ m and width $b_{S_{s,4}} = 400$ m (panels (c) and (d)). Other parameters are shown in Table 1. Panels (a) and (c) show the results of the M2 amplitudes of the tidal elevations, and panels (b) and (d) show the results of the M2 tidal prism. The solid orange curve represents the current reference situation. Blue curves show the effects of the isolated scenarios (see legend). Orange circles and squares show the results of the combination of scenarios 1 and 2, and 1 and 3, respectively.

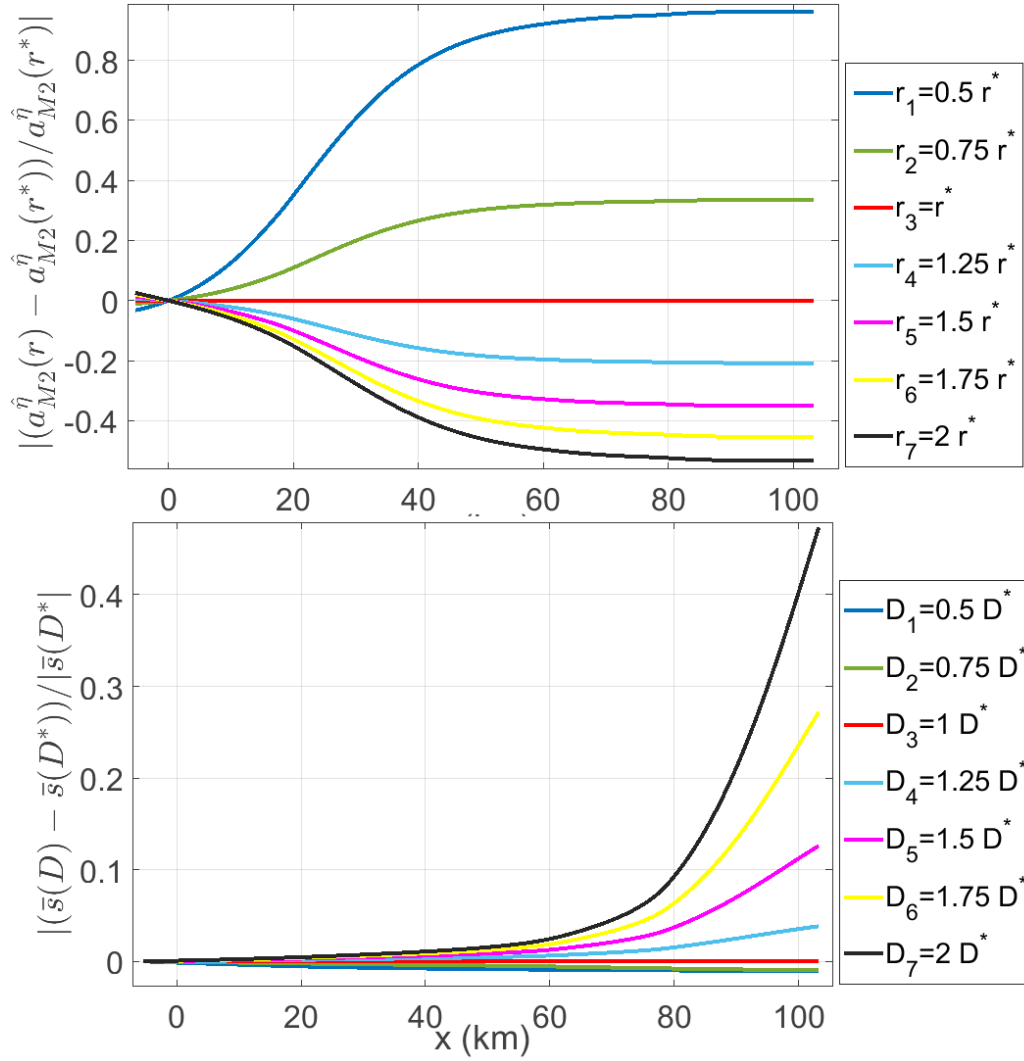


Figure 11: Results of the basic sensitivity analysis. Upper panel: analysis of the relative change of tidal elevations from changes in the friction coefficient. Lower panel: analysis of the relative change of average salinity by varying the dispersion coefficient. Reference values for r^* and D^* are indicated in Table 1.

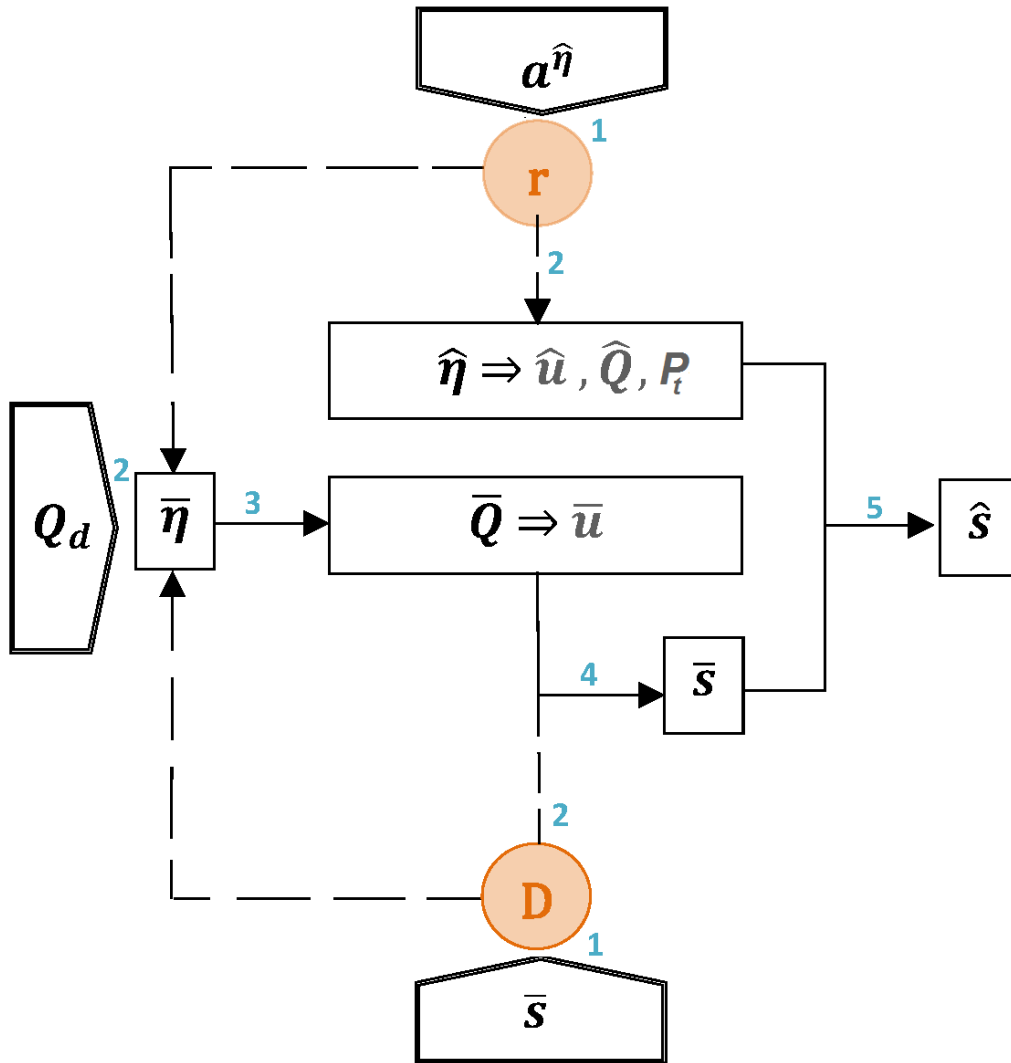


Figure A.12: Procedure diagram to obtain mean and tidal elevations, currents and salinity components, namely, $\{\bar{\eta}, \bar{u}, \bar{s}\}$, and $\{\hat{\eta}, \hat{u}, \hat{s}\}$, respectively. Observations are represented by pentagons, the adjusted parameters with orange circles and the calculated variables with quadrilaterals.